NASA Technical Memorandum 89423

Static Aeroelastic Analysis for Generic Configuration Aircraft

In Lee, Hirokazu Miura, and Mladen K. Chargin

June 1987

NASA

National Aeronautics and
Space Administration

Date for general release _____ June 1989

Static Aeroelastic Analysis for Generic Configuration Aircraft

In Lee,
Hirokazu Miura,
Mladen K. Chargin, Ames Research Center, Moffett Field, California

June 1987

SYMBOLS

A_{ij} = aerodynamic influence coefficient

b = reference length

C_L = lift coefficient

C_p = pressure coefficient

C_r = rolling moment coefficient

D = flexural rigidity of plate

D_{jk} = displacement transformation matrix from "k"-set to "j"-set

f_j^a = pressure on aerodynamic element

F = applied load

F_o = applied load in undeformed condition

F_g = additional aerodynamic load caused by the change from the original deformation

F_k^a = force at aerodynamic control point

G_{kg} = interpolation matrix

k = reduced frequency, $b\omega/V$

$\tilde{K}$ = kernel function

K = system stiffness matrix

K_a = aerodynamic stiffness matrix

K_s = structural stiffness matrix

L = lower triangle with unit elements on diagonal

M = Mach number

p = pressure on aerodynamic surface

P_i = concentrated load at (x_i, y_i)

P_g = grid point force

Q, q = dynamic pressure

r = polar coordinate

R_1 = bending angle, rotation about structural x axis

R_2 = twisting angle, rotation about structural y axis

S = aerodynamic element area

S_{kj} = force transformation matrix from "j"-set to "k"-set

T_3 = displacement in z-direction, normal displacement

u_k = displacement at aerodynamic control point

u_g = displacement at structural grid point

u_r = rigid body displacement

U = upper triangle

V = free-stream velocity

w = downwash (normal wash)

x, y, z = rectangular coordinate system

α = angle of attack

α_i = change in local angle of attack

ξ, η = rectangular coordinate

ϕ = velocity potential

Λ = wing sweep angle

ω = frequency of oscillation

π = 3.141592

SUMMARY

A static aeroelastic analysis capability that can calculate flexible air loads for generic configuration aircraft was developed. It was made possible by integrating a finite element structural analysis code (MSC/NASTRAN) and a panel code of aerodynamic analysis based on linear potential flow theory. The framework already built in MSC/NASTRAN was used and the aerodynamic influence coefficient matrix is computed externally and inserted in the NASTRAN by means of a DMAP program. It was shown that deformation and flexible airloads of an oblique wing aircraft can be calculated reliably by this code both in subsonic and supersonic speeds. Preliminary results indicating importance of flexibility in calculating air loads for this type of aircraft are presented.

INTRODUCTION

The objective of this research is to develop a general static-aeroelastic analysis capability by integrating a panel code for aerodynamic analysis that can cover subsonic as well as supersonic range for both symmetric and asymmetric configuration aircraft into a finite-element structural analysis program. There is no such capability available, except for those imbedded in the proprietary systems used by aircraft manufacturers. In order to make the best use of available resources, a decision was made to use the framework of the MSC/NASTRAN static-aeroelastic analysis capability (refs. 1-3) and to replace the aerodynamic analysis module with the three-dimensional wing code (refs. 4, 5, and private communication of R. Carmichael and I. Kroo), which is applicable to both the supersonic and the subsonic regime, and includes modification to be able to predict the in-plane force caused by the leading-edge suction. Consequently, the capabilities to perform flexible airload calculation and structural wing design for oblique wing aircraft are developed as the results of this study. Various examples were solved to verify the capabilities of the combined system, and program capabilities and limitations were identified.

STATIC AEROELASTICITY

Aerodynamic Theories

Static aeroelasticity is a problem that involves the response of a flexible structure to aerodynamic loading. The analysis of static aeroelasticity involves calculation of static response, including loads and stresses in the structure. In this section, the basic theories involved in this analysis are described. In the

first section, fundamentals of the doublet-lattice method are briefly reviewed because the framework built in MSC/NASTRAN will be used to support this aerodynamic theory. Some number of arrays which are generated externally and which are based upon more appropriate aerodynamic theory will replace the corresponding arrays which are generated by the doublet-lattice theory. In the second section, the aerodynamic theory that provided the basis for the three-dimensional wing code is described.

Doublet Lattice Method- For the aeroelastic analysis, MSC/NASTRAN involves the doublet-lattice method for the subsonic aerodynamic calculation. The doublet-lattice method is used for the calculation of aerodynamic quantities in subsonic flow. This theory is a linearized potential-flow theory which is presented in references 6, 7, and 8. The relation between the normal velocity and pressure at the surface is written as

$$w(x,s) = 1/(8\pi)\iint \tilde{K}(x,\xi;s,\sigma)p(\xi,\sigma)d\xi \; d\sigma \tag{1}$$

where (x,s) are orthogonal coordinates on the surface S as given in figure 1, w is the complex amplitude of dimensionless normal wash, p is the complex amplitude of the lifting pressure coefficient. The complex kernel function is K which includes both vortices and doublets (refs. 6-8).

For computational purposes, the surface is divided into small trapezoidal boxes so that the boxes are arranged in strips which are parallel to the free stream so that the surface edges lie on the box boundaries (fig. 1). It is assumed that the lifting pressure is concentrated along a line. This line is located at the 1/4-chord line of the element. The lifting load line is represented by a horseshoe vortex for its steady effects and a line of doublets for its incremental oscillatory effects. The surface boundary condition is a prescribed normal wash at the control point of each box which is located at the 3/4-chord point along the centerline of each box.

The basic relationship between pressure and downwash (normal wash) is

$$\{w_i\} = (1/q)[A_{ij}]\{p_j\} \tag{2}$$

where

w_i = downwash (normal wash)

p_j = pressure on lifting element

A_{ij} = aerodynamic influence matrix

q = dynamic pressure

The aerodynamic influence coefficient A_{ij} is the magnitude of a normal velocity component that is induced at control point, i, by the jth singularity of unit

strength. This influence matrix is calculated from the following equation (refs. 6-8).

$$A_{ij} = (\Delta C_j / 8\pi) \int_{-d}^{d} \bar{K} \, d\eta \qquad (3)$$

where ΔC_j is the centerline chord of the jth panel and d is its semiwidth, and the kernel function $\bar{K}$ is obtained by concentrating the lifting pressure at the 1/4-chord load line. The flow singularities used to model the lifting surface are steady horseshoe vortices and oscillatory doublets along the bound vortex. Thus, the vortex system represents the steady-flow effects, and the doublets represent the incremental effects of oscillatory motion.

MSC/NASTRAN static aeroelastic analysis is configured so that a user can replace the A_{ij} matrix through a DMAP alter, thus the A_{ij} matrix that is generated outside of MSC/NASTRAN may be substituted for the A_{ij} matrix generated by the doublet-lattice method, as long as these matrices have identical physical meaning and dimensions.

Three-Dimensional Wing Method- The doublet-lattice method used in the MSC/NASTRAN program is not capable of supersonic aerodynamic analysis. The Mach box method (ref. 9) installed in MSC/NASTRAN can be used to estimate aerodynamic forces in supersonic flow. However, this method is applicable only to the symmetric configuration. The other option for supersonic aerodynamics is the piston theory (ref. 10) which is valid in the range of $M = 2.5$ to 7.0. The Mach number range of this oblique wing is in the low supersonic range. Therefore, an alternative aerodynamic code, the three-dimensional wing, was used to calculate the aerodynamic properties in the low supersonic range. In the subsonic range, the results obtained from the three-dimensional wing code agree well with those obtained from the doublet-lattice method.

The three-dimensional wing computer code has been developed by Ralph Carmichael and Ilan Kroo at NASA Ames Research Center. This code was developed based on the theories of references 4 and 5. The three-dimensional wing computer code is used to compute a linear potential flow about a thin wing. The effects of wing thickness are represented by planar source distributions and the effects of wing camber, twist, and incidence effects by planar vortex distributions. The strengths of these singularities are determined so that the resulting flow is tangential to the surface at each control point.

The singularities represent appropriate discontinuities in the u, v, or w velocity components across the wing. The potential function corresponding to each singularity must satisfy the Prandtl-Glauert equation

$$(1 - M^2)\phi_{xx} + \phi_{yy} + \phi_{zz} = 0 \qquad (4)$$

Solutions of equation (4) may be written in integral form. For the planar singularities

3

$$\phi_n = \frac{h}{\pi} \iint \frac{f_n(\xi,\eta)d\xi \, d\eta}{\{(x - \xi)^2 + (1 - M^2)[(y - \eta)^2 + z^2]\}^{1/2}} + \frac{1 - h}{\pi} \iint \frac{z \, d\xi \, d\eta}{(y - \eta)^2 + z^2}$$

$$n = 1,3 \qquad (5)$$

where $h = 0.5$ for $M < 1$, $h = 1.0$ for $M > 1$, and $f_1 = -1$ for constant source distributions, $f_2 = Ln-\xi$ for linearly varying source distributions, and $f_3 = z(x - \xi)/[(y - \eta)^2 + z^2]$ for constant pressure vortex distributions. The second term of equation (5) is included only for constant pressure vortex distributions.

Aerodynamic influence coefficients are also used to calculate the pressures, forces, and moments at subsonic and supersonic speeds. The unknown singularity strengths are determined by the given boundary conditions. This code has been used for the aerodynamic calculation in subsonic and supersonic speeds. The aerodynamic panels are divided into trapezoidal lifting elements as they are in the doublet-lattice method. The aerodynamic influence coefficients calculated from the three-dimensional wing program are used in the NASTRAN program. The aerodynamic influence coefficient matrix is generated in the same format as that generated by the doublet-lattice method described in the previous section. Hence, we can simply replace A_{ij}, which is generated by any of the methods available in MSC/NASTRAN, and all the other framework from that method.

Geometry Interpolation

Aerodynamic Degrees of Freedom- In MSC/NASTRAN, there are two sets of aerodynamic degrees of freedom (ref. 2). One set of degrees of freedom is "j"-set which is a set of degrees of freedom best suited for aerodynamics. The variables for this set are w_j and f_j^a. The variable w_j may include downwash velocities, pitching velocities, angle of attack, camber motions, or any other variable. The force f_j^a may include pressures, moments, and generalized forces and may not necessarily be applied at the same locations as is w_j.

From the aerodynamic theory, we obtain

$$w_j = (1/q)A_{jj}f_j^a \qquad (6)$$

The other set is "k"-set which is a set of degrees of freedom to serve as an interface between the structural degrees of freedom and the "j"-set. The variables for the "k"-set are displacements, u_k, and forces, F_k^a. The displacements and forces must be consistent, so that the product of two corresponding components of force and displacement represents work. The transformation from the k-set to the j-set can be obtained from the following equations.

$$w_j = D_{jk}u_k \qquad (7)$$

4

$$F_k^a = S_{kj} f_j^a \qquad (8)$$

where

u_k, F_k^a = displacement and forces at aerodynamic grid points

f_j^a = pressure on lifting element

There are several ways of choosing the u_k degrees of freedom. For each aerodynamic element, two displacements are chosen in the doublet-lattice method of MSC/NASTRAN. Their locations are the center of pressure and the downwash center. In the subsonic speed, the center of pressure is 1/4 chord and the downwash center is 3/4 chord. Thus, for the doublet-lattice method, the j-set is the downwash at the 3/4 chord and the pressure, and the k-set is the normal displacement at the center of pressure and the normal displacement at the downwash center. Two sets of degrees of freedom are illustrated in figure 2 (ref. 2).

Here, the k-set consists of:

u_{k1}: normal displacement at center of pressure

u_{k2}: normal displacement at downwash center

and j-set consists of:

w_j: downwash at downwash center

f_j^a: pressure coefficient at center of pressure

The s_{kj} matrix is given by

$$\left\{ \begin{matrix} F_{k1}^a \\ F_{k2}^a \end{matrix} \right\} = \begin{bmatrix} S \\ 0 \end{bmatrix} \left\{ f_j^a \right\}$$

where

F_{k1}^a = force at center of pressure

F_{k2}^a = force at downwash center

S = aerodynamic element area

5

The D_{jk} matrix is given by

$$\{w_j\} = \left[\frac{1}{\Delta x} - \left(\frac{1}{\Delta x} + i\frac{k}{b}\right)\right]\begin{Bmatrix} u_{k1} \\ u_{k2} \end{Bmatrix}$$

where

Δx = distance between the center of pressure and the downwash center

b = reference length

k $= \dfrac{b\omega}{V}$

ω = frequency of oscillation

V = free-stream velocity

Surface Spline- There are two sets of displacements for the analysis of the static aeroelasticity in MSC/NASTRAN. One set is the dependent-displacements set, u_k, which is determined at a set of points whose location is determined by the aerodynamic theory. The other set is the independent structural-displacements set, u_g, which consists of structural grid-point displacements in a global coordinate system. The dependent displacements, u_k, are interpolated from the structural displacement u_g by the following relation.

$$\{u_k\} = [G_{kg}]\{u_g\} \tag{9}$$

In order to obtain the interpolation matrix, G_{kg}, we may use three types of splines in MSC/NASTRAN. These are the out-of-plane surface spline, the out-of-plane linear spline, and the inplane linear spline. All splines are planar. Inplane motion consists of displacements which are parallel to the plane and rotations about an axis normal to the plane. Out-of-plane motion consists of displacements normal to the plane, and rotations about axes parallel to the plane. In this study, the out-of-plane displacements (normal displacement) over the wing surface are interpolated by using the above equation (9). Therefore, the out-of-plane surface spline will be used for this analysis.

A surface-spline method is given in reference 11. We will discuss this method in detail for easy understanding of interpolation between structural and aerodynamic grid points which will be discussed in the next section. The surface-spline method is used to find a function $u(x,y)$ for all points (x,y) when u is known for a discrete set of points $u_i = u(x_i,y_i)$. The surface spline is an infinite plate that is deformed by a set of point loads. When a point load P is applied at $r = 0$, the differential equation for a deflection of a plate is

$$D\nabla^4 u = D\frac{1}{r}\frac{d}{dr}\left\{r\frac{d}{dr}\left[\frac{1}{r}\frac{d}{dr}\left(r\frac{du}{dr}\right)\right]\right\} = P \tag{10}$$

6

where r represents a polar coordinate. A solution for the deflection of the plate with many concentrated loads can be obtained by superimposing solutions of equation (10).

$$u(x,y) = b_0 + b_1 x + b_2 y + \sum_{i=1}^{N} K_i(x,y) P_i \tag{11}$$

where

$$K_i(x,y) = (1/16 \ \pi D) r_i^2 \ \ell n \ r_i^2$$

$$r_i^2 = (x_i - x)^2 + (y_i - y)^2$$

$$P_i = \text{concentrated load at } (x_i, y_i)$$

The N + 3 unknowns (b_0, b_1, b_2, P_i, i = 1,N) can be obtained from the N + 3 equations

$$\sum P_i = 0 \tag{12}$$

$$\sum x_i P_i = 0 \tag{13}$$

$$\sum y_i P_i = 0 \tag{14}$$

and

$$u_j = b_0 + b_1 x_j + b_2 y_j + \sum_{i=1}^{N} K_i(x_j,y_j) P_i \quad (j = 1,N) \tag{15}$$

Here, $K_i(x_j,y_j) = K_j(x_i,y_i)$ and $K_i(x_j,y_j) = 0$ when i = j. The unknown variables, u are the displacements at the structural grid points. The unknowns ($b_0, b_1, b_2, P_1, \ldots P_N$) are determined by the following equation.

$$
\begin{Bmatrix} 0 \\ 0 \\ 0 \\ u_1 \\ u_2 \\ \vdots \\ \vdots \\ u_N \end{Bmatrix}
=
\begin{bmatrix}
0 & 0 & 0 & 1 & \cdots & 1 \\
0 & 0 & 0 & x_1 & \cdots & x_N \\
0 & 0 & 0 & y_1 & \cdots & y_N \\
1 & x_1 & y_1 & 0 & \cdots & K_N(x_1,y_1) \\
1 & x_2 & y_2 & K_1(x_2,y_2) & \cdots & K_N(x_2,y_2) \\
\vdots & \vdots & \vdots & \vdots & & \vdots \\
\vdots & \vdots & \vdots & \vdots & & \vdots \\
1 & x_N & y_N & K_1(x_N,y_N) & \cdots & 0
\end{bmatrix}
\begin{Bmatrix} b_0 \\ b_1 \\ b_2 \\ P_1 \\ P_2 \\ \vdots \\ \vdots \\ P_N \end{Bmatrix}
\tag{16}
$$

The interpolation to any point in the plane (x,y) can be determined by evaluating u(x,y) from equation (11).

Interpolation between Structural and Aerodynamic Grid Point- In this analysis, the interpolation between two sets of grid points (aerodynamic and structural) are performed by a spline as described in the previous section. From equation (11), the displacement u can be written as

$$u = [K_1(x,y), K_2(x,y), \ldots, K_N(x,y)] \begin{Bmatrix} P_1 \\ P_2 \\ \cdot \\ \cdot \\ \cdot \\ P_N \end{Bmatrix} + [1,x,y] \begin{Bmatrix} b_o \\ b_1 \\ b_2 \end{Bmatrix} \quad (17)$$

Here, b_o represents a rigid-body displacement (translation in z direction), b_1 represents rigid-body rotation about the y axis, and b_2 represents rigid-body rotation about the x axis. The independent degrees of freedom are the forces applied to the splines at the grid points and the rigid body displacements. The displacement at any point (structural grid or aerodynamic grid) can be written as a linear combination of grid-point forces, P_g, and the rigid-body displacements, u_r.

$$u = [C]\{P_g\} + [R]\{u_r\} \quad (18)$$

where

$[C] = [K_1(x,y), K_2(x,y), \ldots, K_g(x,y)]$

$[R] = [1,x,y]$

$\{u_r\}$ = rigid-body displacement vector

$\{P_g\}$ = grid-point force vector

For the given g-structural grid points, the displacements at structural grid points are obtained from equation (18).

$$\begin{Bmatrix} u_1 \\ u_2 \\ \cdot \\ \cdot \\ \cdot \\ u_g \end{Bmatrix} = \begin{bmatrix} K_1(x_1,y_1) & K_2(x_1,y_1) & \cdots & K_g(x_1,y_1) \\ K_1(x_2,y_2) & K_2(x_2,y_2) & \cdots & K_g(x_2,y_2) \\ \cdot & \cdot & & \cdot \\ \cdot & \cdot & & \cdot \\ \cdot & \cdot & & \cdot \\ K_1(x_g,y_g) & K_2(x_g,y_g) & \cdots & K_g(x_g,y_g) \end{bmatrix} \begin{Bmatrix} P_1 \\ P_2 \\ \cdot \\ \cdot \\ \cdot \\ P_g \end{Bmatrix} + \begin{bmatrix} 1 & x_1 & y_1 \\ 1 & x_2 & y_2 \\ \cdot & \cdot & \cdot \\ \cdot & \cdot & \cdot \\ \cdot & \cdot & \cdot \\ 1 & x_g & y_g \end{bmatrix} \begin{Bmatrix} b_o \\ b_1 \\ b_2 \end{Bmatrix} \quad (19)$$

8

or

$$\{u_g\} = [C_{gg}]\{P_g\} + [R_g]\{u_r\} \qquad (20)$$

If the angular displacements are included in equation (18), the C matrix should be modified. From equations (12), (13), and (14), the equilibrium equations for the structural grid points are

$$\begin{bmatrix} 1 & 1 & \cdots & 1 \\ x_1 & x_2 & & x_g \\ y_1 & y_2 & & y_g \end{bmatrix} \begin{Bmatrix} P_1 \\ P_2 \\ \cdot \\ \cdot \\ \cdot \\ P_g \end{Bmatrix} = \{0\} \qquad (21)$$

This equation can be rewritten as

$$[R_g^T]\{P_g\} = 0 \qquad (22)$$

Thus, for the structural grid points, the following equations are obtained.

$$\begin{Bmatrix} u_g \\ 0 \end{Bmatrix} = \begin{bmatrix} C_{gg} & R_g \\ R_g^T & 0 \end{bmatrix} \begin{Bmatrix} P_g \\ u_r \end{Bmatrix} \qquad (23)$$

For k aerodynamic grid points, the displacement can be given in terms of the structural grid-point forces, P_g and the rigid body displacement, u_r. Thus, from equation (18),

$$\begin{Bmatrix} u_1 \\ u_2 \\ \cdot \\ \cdot \\ \cdot \\ u_k \end{Bmatrix} = \begin{bmatrix} K_1(x_1,y_1) & K_2(x_1,y_1) & \cdots & K_g(x_1,y_1) \\ K_1(x_2,y_2) & K_2(x_2,y_2) & \cdots & K_g(x_2,y_2) \\ \cdot & \cdot & & \cdot \\ \cdot & \cdot & & \cdot \\ \cdot & \cdot & & \cdot \\ K_1(x_k,y_k) & K_2(x_k,y_k) & \cdots & K_g(x_k,y_k) \end{bmatrix} \begin{Bmatrix} P_1 \\ P_2 \\ \cdot \\ \cdot \\ \cdot \\ P_g \end{Bmatrix} + \begin{bmatrix} 1 & x_1 & y_1 \\ 1 & x_2 & y_2 \\ \cdot & \cdot & \cdot \\ \cdot & \cdot & \cdot \\ \cdot & \cdot & \cdot \\ 1 & x_k & y_k \end{bmatrix} \begin{Bmatrix} b_o \\ b_1 \\ b_2 \end{Bmatrix} \qquad (24)$$

or

$$\{u_k\} = [C_{kg}]\{P_g\} + [R_k]\{u_r\} \qquad (25)$$

Combining equations (25) and (23),

$$\{u_k\} = [C_{kg} \quad R_k] \left\{ \begin{array}{c} P_g \\ u_r \end{array} \right\}$$

$$= [C_{kg} \quad R_k] \begin{bmatrix} C_{gg} & R_g \\ R_g^T & 0 \end{bmatrix}^{-1} \left\{ \begin{array}{c} u_g \\ 0 \end{array} \right\}$$

$$= [G_{kg} \quad X] \left\{ \begin{array}{c} u_g \\ 0 \end{array} \right\}$$

$$= [G_{kg}]\{u_g\} \qquad (26)$$

The G_{kg} matrix can be calculated from the following equation.

$$\begin{bmatrix} C_{gg} & R_g \\ R_g^T & 0 \end{bmatrix} \left\{ \begin{array}{c} G_{kg}^T \\ X^T \end{array} \right\} = \left\{ \begin{array}{c} C_{kg}^T \\ R_k^T \end{array} \right\} \qquad (27)$$

Therefore, G_{kg} is determined from two sets of grid points (aerodynamic and structural grid points).

Aerodynamic Force Interpolation

It is necessary to obtain aerodynamic forces applied at the structural grid points because these forces are used in the response solution in the next section. The aerodynamic forces at control points of each element can be obtained by equations (6) through (8).

$$\{F_k^a\} = [S_{kj}]\{f_j^a\} \qquad (8)$$

$$\{f_j^a\} = q[A_{jj}]^{-1}\{w_j\} \qquad (6)$$

and

$$\{w_j\} = [D_{jk}]\{u_k\} \qquad (7)$$

10

where

$\{F_k^a\}$ = vector of aerodynamic forces at aerodynamic control points

$\{f_j^a\}$ = vector of pressure coefficients

$\{w_j\}$ = vector of downwash

$\{u_k\}$ = vector of structural displacements (deformations) at aerodynamic control points

By combining equations (6), (7), and (8), the aerodynamic forces at aerodynamic control points are

$$\{F_k^a\} = q[S_{kj}][A_{jj}]^{-1}[D_{jk}]\{u_k\} \tag{28}$$

The total work should be the same in the two systems (g-set or k-set). Therefore, the following relation should be satisfied.

$$\{u_k\}^T\{F_k^a\} = \{u_g\}^T\{F_g^a\} \tag{29}$$

From equation (26)

$$\{u_k\}^T = \{u_g\}^T[G_{kg}]^T \tag{30}$$

From equations (29) and (30), we obtain the following relationship between the two aerodynamic forces

$$\{F_g^a\} = [G_{kg}]^T\{F_k^a\} \tag{31}$$

Therefore, the aerodynamic forces applied to the structural grid points are derived from equations (28) and (31).

$$\{F_g^a\} = q[G_{kg}]^T[S_{kj}][A_{jj}]^{-1}[D_{jk}][G_{kg}]\{u_g\} \tag{32}$$

Response Solution

The structural equilibrium equation can be written as

$$[K_s]\{u_g\} = \{F\} \tag{33}$$

where $[K_s]$ is the structural stiffness matrix, $\{u_g\}$ is the displacement, and $\{F\}$ is the applied load. The forces and moments can be represented by

$$\{F\} = \{F_o\} + \{F_g\} \tag{34}$$

11

where $\{F_o\}$ is the applied load in the undeformed condition, and $\{F_g\}$ is the additional load caused by the change from the original deformation. From the previous section, the aerodynamic force vector as it is applied at structural grid points can be expressed as

$$\{F_g\} = q[G_{kg}]^T[S_{kj}][A_{jj}]^{-1}[D_{jk}][G_{kg}]\{u_g\} \tag{35}$$

The force F_o is composed of two loads.

$$\{F_o\} = \{F_{ss}\} + \{F_s\} \tag{36}$$

where

$\{F_{ss}\}$ = structural load

$\{F_s\}$ = static aerodynamic force; primarily, the force which is determined by the jig shape of the wing and the angle of attack.

The flexible wing geometry can be expressed in terms of translational and rotational deflections

$$\{u\} = \{u_o\} + \{u_g\} \tag{37}$$

where $\{u_o\}$ is the undeformed jig shape and $\{u_g\}$ is the elastic deformation at the structural grid points.

From equations (33) through (35), we obtain

$$[K_s]\{u_g\} = \{F_o\} + q[G_{kg}]^T[S_{kj}][A_{jj}]^{-1}[D_{jk}][G_{kg}]\{u_g\} \tag{38}$$

Rearranging the above equation, we get

$$[K]\{u_g\} = \{F_o\} \tag{39}$$

where the system stiffness matrix $[K]$ is defined as

$$[K] = [K_s] - [K_a] \tag{40}$$

and the aerodynamic stiffness matrix, $[K_a]$ is defined as

$$[K_a] = q[G_{kg}]^T[S_{kj}][A_{jj}]^{-1}[D_{jk}][G_{kg}] \tag{41}$$

We can obtain the aeroelastic response from equation (39). The standard procedure for solving equation (39) is to decompose $[K]$ into its triangular factors

$$[K] = [L][U] \tag{42}$$

12

where [L] is a lower triangle with unit elements on the diagonal and [U] is an upper triangle. Then, equation (39) can be rewritten as

$$[L]\{y\} = \{F_o\} \tag{43}$$

and

$$[U]\{u_g\} = \{y\} \tag{44}$$

The solution of equation (43) for {y} is obtained by the forward substitution, and the subsequent solution of equation (44) is obtained by the backward substitution.

The above solution may require a significant amount of computer time because the aerodynamic stiffness matrix $[K_a]$ is relatively full, when compared to $[K_s]$. In such cases, an iterative procedure may be more efficient. From equation (39), we can formulate the iteration procedure.

$$[K_s]\{u_g^n\} = \{F_o\} + [K_a]\{u_g^{n-1}\} \tag{45}$$

where $\{u_g^n\}$ is the nth iterate.

RESULTS AND DISCUSSION

Sample Problems

<u>Swept-Back Wing</u>- As a first problem, a 45° swept-back flat-plate wing has been analyzed. The structural elements and aerodynamic elements are shown in figures 3 and 4, respectively. The structural and aerodynamic panels are both two-dimensional. The wing span is 600 in. and its chord length is 200 in. The structural thickness of the aluminum wing plate is 2 in.; however, aerodynamically the wing is assumed to be a thin panel. In this case, the dynamic pressure is 2 psi and the angle of attack is 10°.

The clamped boundary condition is given along a line AB in figure 3. The structural displacements are given in figure 5. Because of the symmetric air loading, the displacements in the z-direction are symmetrical with respect to x-z plane. The trailing edge has more deflection than the leading edge does since the wing has a larger moment arm about the reference pitch axis near the trailing edge.

The aerodynamic forces have been calculated with the doublet-lattice method installed in MSC/NASTRAN and also with the aerodynamic influence coefficients obtained by using the three-dimensional wing program. Throughout this report, the doublet-lattice method has been used to calculate the subsonic aerodynamic quantities. The three-dimensional wing code was shown to be a reliable computer code by comparing its results and those of the doublet lattice code, and it has been used exclusively to calculate supersonic aerodynamic quantities. The results of the two

analyses virtually agreed. The comparison between two results is given in the section on the 250-ft^2 oblique wing.

Table 1 gives the accuracy for several different interpolation regions. In the appendix, the interpolation regions are explained. Figure 6 shows the surface-spline regions used in this analysis. Figure 6(a) shows 2 spline regions, figure 6(b) shows 4 regions, and figure 6(c) shows 6 regions. The maximum difference for the maximum deflection is only 0.2% for the above cases. Therefore, the number of aerodynamic elements in a surface-spline region does not significantly affect the results.

Oblique Wing-I- As a second problem, a simple, asymmetric flat-plate wing with a sweep angle of 45° has been analyzed. This wing has been chosen as a preliminary model for a more complicated oblique wing.

The structural and aerodynamic elements are shown in figures 7 and 8, respectively. Both the structural and aerodynamic panels are two-dimensional with a wing span of 600 in. and a chord length of 200 in. As in the previous case, the aluminum plate thickness is 2 in. In this case, the dynamic pressure is 0.3 psi and the angle of attack is 10°.

The clamped boundary condition is along line AB in figure 7. The structural displacements are given in figure 9. The left-side wing has more loading than the right-side wing does because the left-side wing has more upwash than the right-side wing. However, the right-side wing has more pitching moment about the y-axis than the left-side wing does because the bigger loads are applied near the leading edge of the wing. Therefore, the displacement pattern of the oblique wing is quite different from that of the swept-back wing. The right wing is twisted to increase the local angle of attack whereas the left wing is twisted to decrease the local angle of attack.

Table 2 gives the accuracy for two different interpolation regions. Figure 10 shows the spline regions used in this analysis. Figure 10(a) shows 2 spline regions, and figure 10(b) shows 6 regions. The maximum difference for the maximum deflection is only 0.25% for the above cases. Therefore, as seen before, the number of aerodynamic elements in a surface-spline region does not significantly affect the results.

Oblique Wing-II- As a third problem, another two-dimensional oblique wing with total area of 250 ft^2 has been analyzed. Several different numbers of aerodynamic and structural elements (table 3) are used for the calculation. Among them, the typical structural elements and aerodynamic elements are given in figures 11 and 12, respectively. Both the structural and aerodynamic panels are two-dimensional. The aluminum plate thickness is again 2 in. In this case, the dynamic pressure is 0.5 psi and the angle of attack is 10°.

The clamped boundary condition is along line AB in figure 11. The structural displacements are given in figure 13. As in the case for the oblique wing I, the left-side wing has more lift than does the right-side wing. However, the wing tip

of the right-side wing has more deflection than the left-side wing does because of the different moment pattern. The general deflection pattern for this wing is similar to that for the previous case.

Table 3 shows the relation between the maximum deflection and the number of aerodynamic and structural elements. The number of aerodynamic elements affects structural deformation more significantly than does the number of structural elements. For almost the same number of aerodynamic elements (136 and 144), the maximum deflection is almost the same (only 0.1% difference) when increasing the number of structural elements (from 56 to 132). Maximum deflection occurs at the tip of the right-side wing. However, the maximum deflection decreases by 4.2% when increasing the number of aerodynamic elements from 144 to 224, also decreases by 5.7% when increasing the number of aerodynamic elements from 144 to 336. We can see that the more aerodynamic elements there are, the more accurate the prediction is for aerodynamic forces over the wing surface. Therefore, we should have enough aerodynamic elements to predict the correct aerodynamic forces. Near the leading-edge and wing-tip regions, the pressure variations are very steep, and fine aerodynamic meshes are required.

Figure 14(a) shows 7 surface-spline regions where the number of aeroelements is 136 and figure 14(b) shows 11 surface-spline regions where the number of aeroelements is 336.

Oblique Wing (250 ft^2)

In this section, we will discuss the full-scale 250-ft^2 oblique wing. Also, we will examine a rigid oblique wing and flexible-optimized wing to show the wing flexibility effect. The structural elements of the upper surface are shown in figures 15(a) and 15(b). The aerodynamic elements are given in figure 16. The analyzed structural shape is three-dimensional. For the aerodynamic analysis, zero-thickness panels are used. However, the total lift will not be very different from that obtained by three-dimensional aerodynamic calculation because the wing is a thin airfoil. The thickness ratio of the airfoil at the centerline is 14% and linearly decreases to 12% at the 85% semispan station. The sweep angle of the wing is 65°.

Baseline Oblique Wing (250 ft^2)- As a first problem for the full-scale oblique wing, we consider an oblique wing of which the area is 250 ft^2. The pin-jointed boundary conditions are given at the four structural grid points. These points are structural grid numbers 202, 219, 602, and 619, and they are located on the lower surface of the wing. The corresponding structural grid numbers on the upper surface are 102, 119, 502, and 519 and are shown in figures 15(a) and 15(b).

The structural deformations are shown in figures 17(a) and 17(b). Figure 17(a) gives a three-dimensional view and figure 17(b) shows another view of oblique wing. As in the previous case, the right-side wing has more displacements than the left-side wing. The aerodynamic pressure distributions are given in figure 18. Here, the pressure is a differential pressure (lower surface pressure-upper surface pressure). Near the leading edge, the high pressures are developed. In the case of

15

the rigid wing, the left-side wing has more lift than the right-side wing does because the left-side wing is subjected to the stronger upwash which is developed by the right-side wing. In this case, the Mach number is 0.7 and the angle of attack is 10°. The solid curve represents pressure distributions of the baseline oblique wing, and the dashed curves represent pressure distributions of the optimized wing which is more flexible than the baseline wing. For the left-side wing, the baseline wing has more loading than the optimized (flexible) wing does. However, for the right-side wing, the optimized wing has more loading than the baseline wing does. The difference in loading pattern causes a change in the rolling moment, and reflects the wing's flexibility.

The comparison between the doublet-lattice method and the three-dimensional wing program results is given in table 4. The total lift is almost the same between the two methods (0.4% differences). However, the maximum deflection has more difference (5.5%). The rolling-moment coefficient has some difference but these values are relatively small. For the interpolation of structural displacements, 11 surface-spline regions are used. The surface spline regions are shown in figure 14(b).

Table 5 gives subsonic characteristics of the oblique wing according to the various Mach numbers (0.4, 0.5, 0.6, and 0.7) at a fixed angle of attack (10°). Here, the load factors are calculated based on the value of aircraft gross weight as 24,000 lb. The lift coefficient changes are very small in the subsonic region. Compared with the results of the rigid wing given in the section on the rigid wing, the lift coefficient of this wing is slightly larger than that of the rigid wing. The rolling-moment coefficient increases with the increase in the Mach number. These two effects can be explained by the wing flexibility. We will discuss these flexibility effects in the section on the rigid wing and the optimized wing. As expected, the maximum vertical deflection increases when the lift force increases and occurs at the tip of the right-side wing.

Table 6 shows the results for the three different angles of attack. The calculated angles of attack are 4.22, 10, and 15°. For this range of angle of attack, the lift curve is in the linear region. The rolling-moment coefficient also decreases linearly with the angle of attack. We can see the maximum deflection varies almost linearly with the angle of attack.

Table 7 shows supersonic characteristics of the oblique wing. The aerodynamic influence coefficients are calculated from the three-dimensional wing computer code. In this supersonic speed, the sign of rolling moment changes from negative to positive. That is, because of the wing-flexibility effect, the right wing has more lift than the left wing. The angle of attack of the right wing (sweep-forward wing) increases whereas that of the left wing (sweep-backward wing) tends to decrease.

Rigid Wing- Table 8 gives the rigid-wing characteristics for the oblique wing. The rigid-wing results were obtained by increasing E (Young's modulus) and G (Shear modulus) by 100 times. For this rigid wing, both the lift coefficients and rolling-moment coefficients are nearly constant with the increase in the Mach number. Therefore, we can say that there is no flexibility effect in this case.

16

Table 9 shows the rigid-wing results for the three different angles of attack. The calculated angles of attack are 4.22, 10, and 15°. For this range of angle of attack, the lift curve is in the linear region. However, the lift-curve slope decreases with the increase of wing rigidity as expected. The rolling-moment coefficient also decreases linearly with the angle of attack.

Optimized Wing- In this section, we will discuss a strength-designed wing to show the significant static aeroelastic effects on the wing displacements and the aerodynamic quantities. The 250-ft^2 oblique wing described in the section on the baseline oblique wing has been analyzed to show that it can withstand the composite thickness for 4-g maneuvering condition. The criteria are applied to longitudinal and shear strains for each of the 0, 45, and 90° piles. No stability criteria were considered. The optimum composite wing-plate thickness distributions are given in table 10. Span station 1 is the location number for the panel near the wing root and span station 14 is for the panel near the wing tip. The structural elements and aerodynamic elements are the same as those for the 250-ft^2 baseline oblique wing given in the previous section.

Table 11 shows the static aeroelastic effects for the oblique wing. In this case, the angle of attack is 15° and the Mach number is 0.7. The 250-ft^2 oblique wing has 2.3% more lift than the rigid wing does and the optimized wing has 7.8% more lift than the rigid wing. There is a significant change in the deflection of the optimized wing. The maximum deflection is 34.22 in. for the optimized wing and it is 14.66 in. for the unoptimized wing (baseline 250-ft^2 wing). The rolling-moment coefficient is positive for the optimized (flexible) wing and is negative for the others. The big change in this coefficient shows the significance of wing flexibility on aerodynamic load distribution.

Table 12 gives the subsonic characteristics for the optimized wing. The lift coefficients are no longer constant for this flexible wing. With the increase of the Mach number (dynamic pressure), both the lift coefficient and rolling-moment coefficient increase. This reflects the wing flexibility again. Between the Mach number, 0.5 and 0.6, the sign of rolling-moment coefficient changes from negative to positive.

Discussions on Oblique Wing Analysis

Aerodynamic Coefficients- In this section, the previous results are summarized. Figure 19 shows the lift coefficient versus the Mach number in the subsonic region. The sea level conditions are used for the calculations. The angle of attack is 10° and the optimized (flexible) wing has the biggest lift. The flexibility effects increase with the increase of Mach number for both the baseline oblique wing and the optimized wing. When the Mach number is 0.7, the lift coefficient of the optimized wing is 7.8% higher than that of the rigid wing and the coefficient of the baseline oblique wing is 5.4% higher than that of the rigid wing.

17

Figure 20 shows the lift-curve slopes for three wings at a Mach number of 0.7. Although the wing is flexible, the lift coefficient is still linear for this range of angle of attack. The most flexible wing has more lift than the others as expected.

Figure 21 shows the rolling-moment coefficient versus the angle of attack. The calculated Mach number is 0.7. The rolling-moment coefficients are negative for both the baseline oblique wing and the rigid wing, and they are positive for the optimized (flexible) wing. The rolling-moment coefficients are also linear for this range of angle of attack. For the optimized wing, wing flexibility gives a large change in the rolling moment which is attributed to the increase of the local angle of attack in the right-side wing, and the decrease of local angle of attack in the left-side wing. One example for the local angle of attack calculation is given for both the baseline oblique wing and the optimized wing in the next section.

Figure 22 shows the rolling moment coefficient versus the Mach number. The angle of attack is 10°. Substantial differences in the rolling moment caused by wing flexibility are observed. For the rigid wing, the rolling moments are almost constant but they tend to decrease slightly with the increase of Mach number. For this rigid wing, the effective angle of attack is strongly affected by the upwash. As we explained in the previous section, the upwash of the left-side wing (swept-back wing) is larger than that of the right-side wing (swept-forward wing). This effect results in the negative rolling moment for the rigid wing. As the angle of attack increases, this upwash effect increases and the rolling moment decreases for the rigid wing as illustrated in figure 21. We can see the same effect in figure 20. As the Mach number increases, the rolling moment decreases slightly for the rigid wing.

Local angle of attack- In this section, we will discuss the local angle of attack change caused by the change of wing bending as well as torsion to examine the local effect of flexibility. For the flexible wing, depending on the span and chord position of the wing, both torsion and bending angles vary. The magnitude of the bending angle is maximum at the wing tip. We now examine the local angle-of-attack change at the 74% semispan station in the structural coordinates for both the right-side and the left-side wings. These span stations are shown in figure 15(a) (section B-B) and in figure 15(b) (section A-A). The Mach number is 0.7 and R1 is the bending angle, or rotation about the x-axis and R2 is the twisting angle, or rotation about the y-axis where the x and y axes are defined in the structural coordinates. The positive bending angle occurs when the right-side wing is up and the left-side wing is down. Also, the positive twisting angle occurs when the wing is in the positive pitch angle (nose-up).

Figure 23 shows the bending angle, R1 at the given 74% semispan station. The optimized wing has a bigger bending angle than the baseline oblique wing. For the optimized wing, the magnitude of the bending angle of the right-side wing is more than two times higher than that of the left-side wing. For the general wing structure, the magnitude of bending angle is bigger than that of the twisting angle at a given wing position. For this high-sweep angle (65°), this big bending angle results in the big change of local angle of attack.

Figure 24 shows the twisting angle, R2 at the 74% semispan station. As expected, the optimized wing has more twisting angle than the baseline oblique wing. The magnitude of the twisting angle of the right-side wing is nearly two times more than that of the left-side wing for the optimized wing and is 30 to 40% more than that of the left-side wing according to the chord position for the baseline oblique wing.

From these two angles, we can calculate the local angle-of-attack change. The local angle of attack change, α_i, is

$$\alpha_i = R_1 \sin \Lambda + R_2 \cos \Lambda$$

where Λ is the wing sweep angle. Figure 25 shows the local angle-of-attack change. The given angle of attack is 10°. At 74% semispan station, the local angle of attack of the right-side wing is around 12.7° and that of the left-side wing is around 8.6° for the baseline oblique wing. For the same span station of the optimized wing, the local angle of attack of the right-side wing is about 16.8° and that of the left-side wing is about 7.6°. This difference in the angle of attack results in the positive rolling moment for the optimized wing. Thus, the flexibility of wing makes the significant difference in the local angle of attack and aerodynamic characteristics and especially for the rolling-moment characteristics.

Figure 26 shows the vertical displacement, T3 at the 74% semispan station. The vertical displacement of the right-side wing is more than two times bigger than that of the left-side wing in the optimized wing. For the same span station of the baseline oblique wing, this displacement of the right-side wing is about 60% bigger than that of the left-side wing.

CONCLUSIONS

A static-aeroelastic analysis capability has been developed that is applicable to unsymmetric aircraft configuration including the oblique wing for both subsonic and supersonic regimes.

Significances of wing flexibility are analyzed for the three different oblique wings (very rigid wing, 250-ft^2 baseline wing, and optimized flexible wing). The aerodynamic influence coefficients are calculated using both the doublet-lattice method and the three-dimensional wing computer code to obtain the aerodynamic forces. These two results are very close and are considered very reliable for similar applications.

The supersonic capability for static aeroelasticity has been developed by combining the three-dimensional wing program and the MSC/NASTRAN computer program.

The increase of the number of aerodynamic elements affects the structural deformation results more significantly than the increase of the number of structural elements does.

The wing flexibility changes the local angles of attack, the load distribution over the entire wing, and has the most significant effects on the rolling moment.

APPENDIX

INTERPOLATION PROCEDURE

In this analysis, a surface spline is used to interpolate the displacements at the aerodynamic control points, u_k, from the displacement at the structural grid points.

To perform the surface-spline interpolation, SPLINE1 and SET1 or SET2 CARDS are used in MSC/NASTRAN. As an example, aerodynamic and structural grids are given in figure 27. In this figure, the SPLINE1 card defines an interpolated aerodynamic region which is a shaded region in this figure. The interpolated region involves aerodynamic elements from 101 to 108. The SET2 CARD defines a set of structural grid points within the region defined by the SPLINE1 CARD. The SET1 CARD defines the structural grid points directly. Because we defined the interpolated region (aerodynamic elements 101 to 108) as the shaded region, the structural grid points (1,2,...,8) are included in the shaded region as part of the aerodynamic elements. Thus, the interpolations can be performed from the following equation.

$$\{u_k\} = [G_{kg}]\{u_g\}$$

Here, G_{kg} can be determined only from the two sets of grid points. In version 64A of MSC/NASTRAN, there is a limitation for the maximum number of aerodynamic elements in one spline region which is 48. However, this limitation has been removed in version 65A.

REFERENCES

1. Rodden, W. P.; Harder, R. L.; and Bellinger, E. D.: Aeroelastic Addition to NASTRAN, NASA CR-3094, Mar. 1979.

2. Harder, R. L.; MacNeal, R. H.; and Rodden, W. P.: A Design Study for the Incorporation of Aeroelastic Capability into NASTRAN. NASA CR-111918, Aug. 1965.

3. Rodden, W. P.; Wilson, C. T.; Herting, D. N.; Bellinger, E. D.; and MacNeal, R. H.: Static Aeroelastic Addition to MSC/NASTRAN. Paper 15, Proceedings of the 1984 MSC/NASTRAN User's Conference, Pasadena, CA, Mar. 1984.

4. Woodward, F. A.; Tinoco, E. N.; and Larsen, J. W.: Analysis and Design of Supersonic Wing-Body Combinations, Including Flow Properties in the Near Field, Part I--Theory and Application. NASA CR-73106, Aug. 1967.

5. Woodward, F. A.: Analysis and Design of Wing-Body Combinations at Subsonic and Supersonic Speeds. J. of Aircraft, vol. 5, no. 6, Nov.-Dec. 1968, pp. 528-534.

6. Albano, E.; and Rodden, W. P.: A Doublet-Lattice Method for Calculating Lift Distributions on Oscillating Surfaces in Subsonic Flows. AIAA J., vol. 7, no. 2, Feb. 1969, pp. 279-285, and vol. 7, no. 11, Nov. 1969, p. 2192.

7. Rodden, W. P.; Giesing, J. P.; and Kalman, T. P.: New Developments and Applications of the Subsonic Doublet-Lattice Method for Nonplanar Configurations. AGARD-CP-80-71, Paper 4, AGARD Symposium on Unsteady Aerodynamics for Aeroelastic Analyses of Interfering Surfaces, Tonsberg, Oslofjorden, Norway, Nov. 1970.

8. Rodden, W. P.; Giesing, J. P.; and Kalman, T. P.: Refinement of the Nonplanar Aspects of the Subsonic Doublet-Lattice Lifting Surface Method. J. Aircraft, vol. 9, no. 1, Jan. 1972, pp. 69-73.

9. Pines, S.; Dugundji, J.; and Neuringer, J.: Aerodynamic Flutter Derivatives for a Flexible Wing with Supersonic and Subsonic Edges. J. Aero. Sci., vol. 22, no. 10, Oct. 1955, pp. 693-700.

10. Ashley, H.; and Zartarian, G.: Piston Theory--A New Aerodynamic Tool for the Aeroelastician. J. Aero. Sci., vol. 23, no. 12, Dec. 1956, pp. 1109-1118.

11. Harder, R. L.; and Desmarais, R. N.: Interpolation Using Surface Splines. J. of Aircraft, vol. 9, no. 2, Feb. 1972, pp. 189-191.

TABLE 1.- COMPARISON OF MAXIMUM DEFLECTION FOR THE DIFFERENT SURFACE
SPLINE REGIONS FOR SWEPT-BACK FLAT-PLATE WING

Number of surface spline region	Number of aero-elements within one spline region	Number of structural grid points within one spline region	Maximum deflection, in.
2 (fig. 6(a))	45	35	116.19
4 (fig. 6(b))	20 - 25	15 - 20	116.43
6 (fig. 6(c))	15	15	116.35

TABLE 2.- COMPARISON OF MAXIMUM DEFLECTION FOR THE DIFFERENT SURFACE
SPLINE REGIONS FOR OBLIQUE WING I

Number of surface spline region	Number of aero-elements within one spline region	Number of structural grid points within one spline region	Maximum deflection, in.
2 (fig. 10(a))	45	35	127.18
6 (fig. 10(b))	15	15	127.50

TABLE 3.- COMPARISON OF MAXIMUM DEFLECTION
FOR THE DIFFERENT AERO AND STRUCTURAL
ELEMENTS

Number of structure elements	Number of aero-elements	Number of spline regions	Maximum deflection, in.
56	136	7	21.02
88	224	8	20.15
132	144	8	21.04
132	336	11	19.84

TABLE 4.- COMPARISON BETWEEN DOUBLET-LATTICE METHOD AND THREE-DIMENSIONAL WING PROGRAM

Variables	Doublet lattice	Three-dimensional wing
Mach number	0.7	0.7
Dynamic pressure, psi	5.047	5.047
Angle of attack, deg	10.0	10.0
Total lift, lb	56876	57100
Lift coefficient	0.313	0.314
Rolling moment, lb-in.	-70916	-95973
Rolling moment coefficient	-0.0015	-0.0020
Maximum deflection, in.	9.773	9.239

TABLE 5.- SUBSONIC CHARACTERISTICS FOR THE OBLIQUE WING

Variables	Mach number			
	0.4	0.5	0.6	0.7
Angle of attack, deg	10	10	10	10
Dynamic pressure, psi	1.648	2.575	3.708	5.047
Total lift, lb	17795	28071	40979	56876
Lift coefficient	0.300	0.303	0.307	0.313
Rolling moment, lb-in.	-87885	-111495	-112776	-70916
Rolling moment coefficient	-0.0057	-0.0046	-0.0033	-0.0015
Load factor	0.74	1.17	1.71	2.37
Maximum deflection, in.	2.685	4.385	6.684	9.773

TABLE 6.- OBLIQUE WING CHARACTERISTICS FOR ANGLE-OF-ATTACK CHANGE

Variables	Mach number 0.7		
Dynamic pressure, psi	5.047	5.047	5.047
Total lift, lb	24000	56876	85331
Lift coefficient	0.132	0.313	0.470
Rolling moment, lb-in.	-29925	-70916	-106394
Rolling moment coefficient	-0.00063	-0.00150	-0.00226
Load factor	1.0	2.37	3.55
Maximum deflection	4.124	9.773	14.663

TABLE 7.- SUPERSONIC CHARACTERISTICS FOR THE
OBLIQUE WING

Variables	Mach number	
	0.7	1.6
Dynamic pressure, psi	5.047	6.944
Angle of attack, deg	10.0	10.0
Total lift, lb	57100	96182
Lift coefficient	0.314	0.385
Load factor	2.379	4.008
Rolling moment, lb-in.	-95973	95274
Rolling moment coefficient	-0.0020	0.0015
Maximum deflection, in.	9.239	15.481

TABLE 8.- RIGID WING CHARACTERISTICS FOR OBLIQUE WING

Variables	Mach number			
	0.4	0.5	0.6	0.7
Dynamic pressure, psi	1.648	2.575	3.708	5.047
Angle of attack, deg	10.0	10.0	10.0	10.0
Total lift, lb	17744	27894	40475	55604
Lift coefficient	0.299	0.301	0.303	0.306
Load factor	0.739	1.162	1.686	2.317
Rolling moment, lb-in.	-120645	-193050	-286510	-404874
Rolling moment coefficient	-0.0078	-0.0080	-0.0083	-0.0086
Maximum deflection, in.	0.025	0.039	0.057	0.077

TABLE 9.- RIGID WING CHARACTERISTICS FOR ANGLE-OF-ATTACK CHANGE

Variables	Mach number 0.7		
Angle of attack, deg	4.22	10.0	15.0
Dynamic pressure, psi	5.047	5.047	5.047
Total lift, lb	23462	55604	83422
Lift coefficient	0.129	0.306	0.459
Rolling moment, lb-in.	-170836	-404874	-607428
Rolling moment coefficient	-0.0036	-0.0086	-0.0129
Load factor	0.98	2.32	3.48

TABLE 10.- THICKNESS DISTRIBUTION FOR THE BASELINE OBLIQUE
WING AND OPTIMIZED WING

Span Station	Baseline wing, 250 ft^2			Optimized wing		
	Composite ply angle			Composite ply angle		
	0	45	90	0	45	90
1	0.53125	0.04375	0.05000	0.25118	0.00617	0.00617
2	0.48970	0.04370	0.04960	0.27965	0.00733	0.00665
3	0.45700	0.04410	0.04960	0.28811	0.00871	0.00619
4	0.42200	0.04380	0.04890	0.23187	0.01096	0.00602
5	0.38300	0.04260	0.04730	0.20942	0.00880	0.00583
6	0.34000	0.04250	0.04250	0.18400	0.00774	0.00525
7	0.29400	0.04140	0.03730	0.16072	0.00730	0.00500
8	0.26200	0.04130	0.03290	0.13904	0.00722	0.00500
9	0.23400	0.04120	0.02960	0.11275	0.00635	0.00500
10	0.20800	0.04470	0.02540	0.08309	0.00600	0.00500
11	0.18450	0.04550	0.02200	0.05393	0.00582	0.00500
12	0.15900	0.04420	0.01770	0.02727	0.00545	0.00500
13	0.14200	0.04300	0.01500	0.01724	0.00533	0.00500
14	0.12880	0.04232	0.01288	0.01577	0.00572	0.00500

TABLE 11.- STATIC AEROELASTIC EFFECTS ON THE OPTIMIZED WING

Variables	Mach number 0.7		
	Rigid wing	Baseline, 250 ft^2	Optimized wing
Dynamic pressure, psi	5.047	5.047	5.047
Angle of attack, deg	15	15	15
Total lift, lb	83422	85331	89978
Lift coefficient	0.459	0.470	0.495
Load factor	3.476	3.555	3.749
Rolling moment, lb-in.	-607428	-106394	410050
Rolling moment coefficient	-0.0129	-0.0023	0.0087
Maximum deflection	0.11[a]	14.66	34.22

[a]This maximum deflection has been calculated again based on the value of 100 times of E and G as in the previous section and should be zero for a perfectly rigid wing.

TABLE 12.- SUBSONIC CHARACTERISTICS FOR OPTIMIZED OBLIQUE WING

Variables	Mach number			
	0.4	0.5	0.6	0.7
Dynamic pressure, psi	1.648	2.575	3.708	5.047
Angle of attack, deg	10.0	10.0	10.0	10.0
Total lift, lb	17896	28435	42093	59974
Lift coefficient	0.302	0.307	0.315	0.330
Load factor	0.746	1.185	1.754	2.499
Rolling moment, lb-in.	-60009	-39669	49523	273314
Rolling moment coefficient	-0.0039	-0.0017	0.0014	0.0058
Maximum deflection, in.	5.259	8.928	14.384	22.808
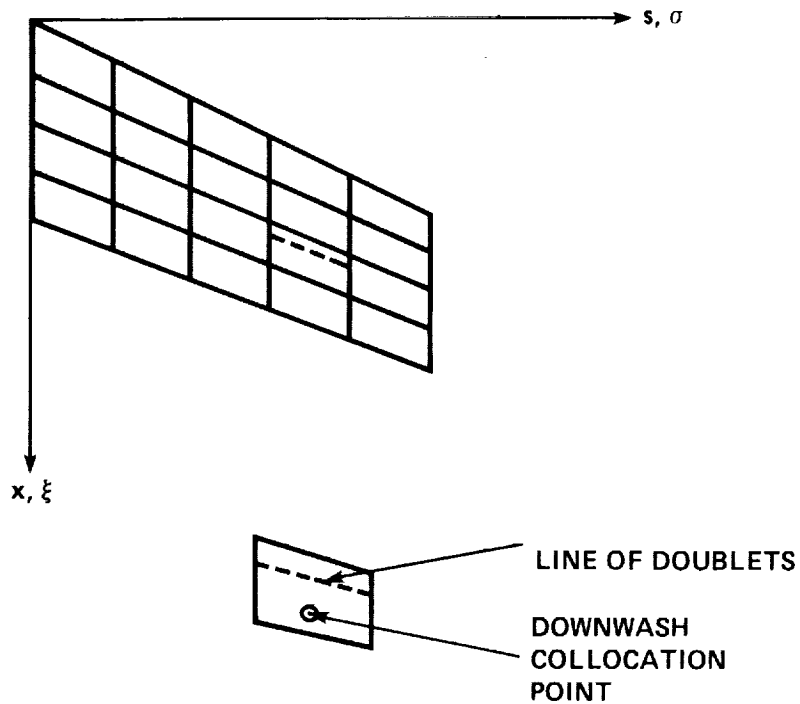
Figure 1.- Aerodynamic elements and location of doublets and collocation
points for doublet-lattice method (ref. 8).
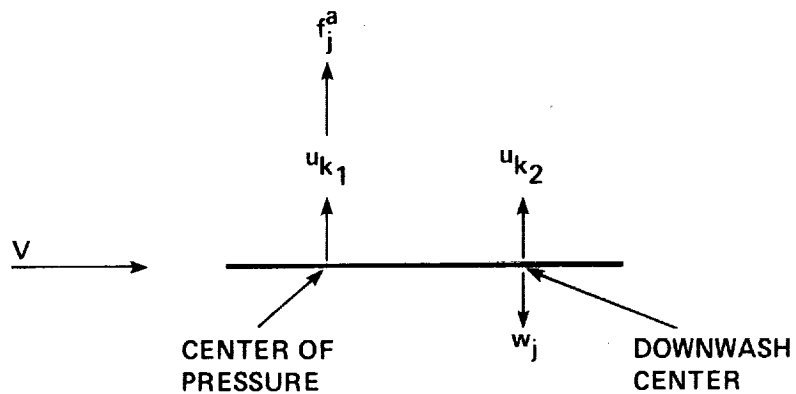
Figure 2.- Illustration of aerodynamic degrees of freedom.
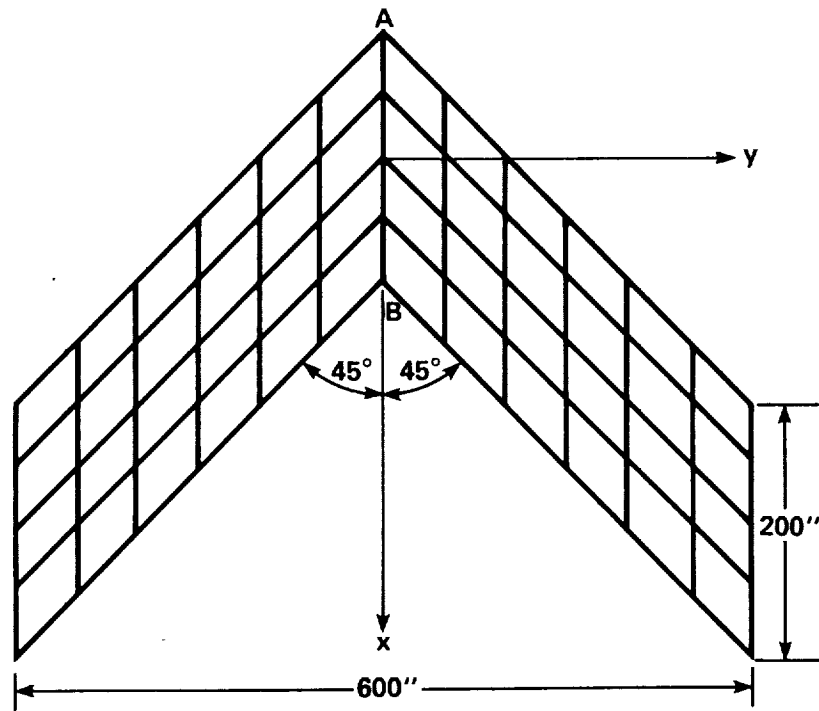
Figure 3.- Structural grid for swept-back wing.
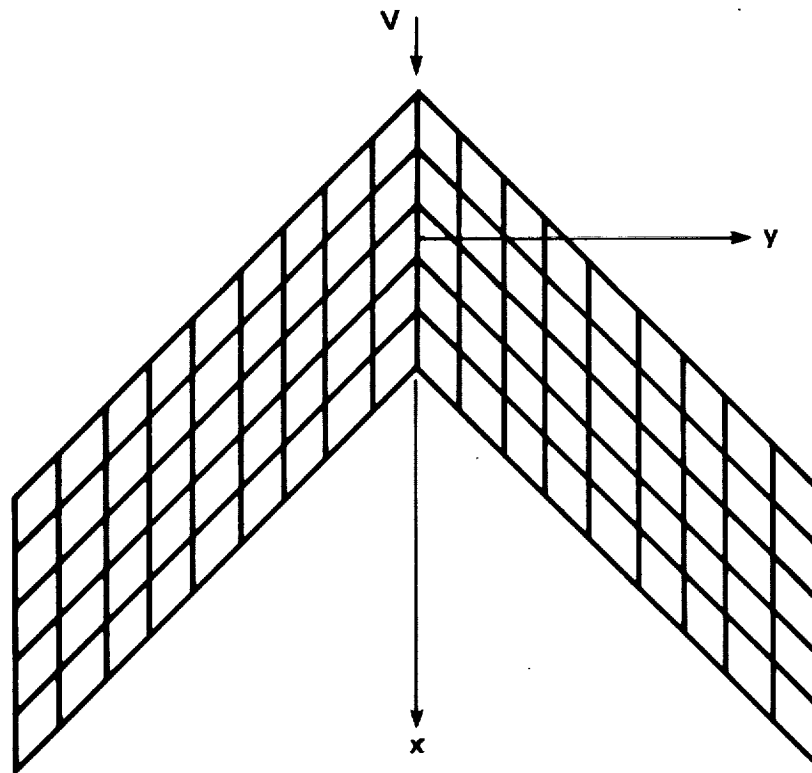
Figure 4.- Aerodynamic grid for swept-back wing.
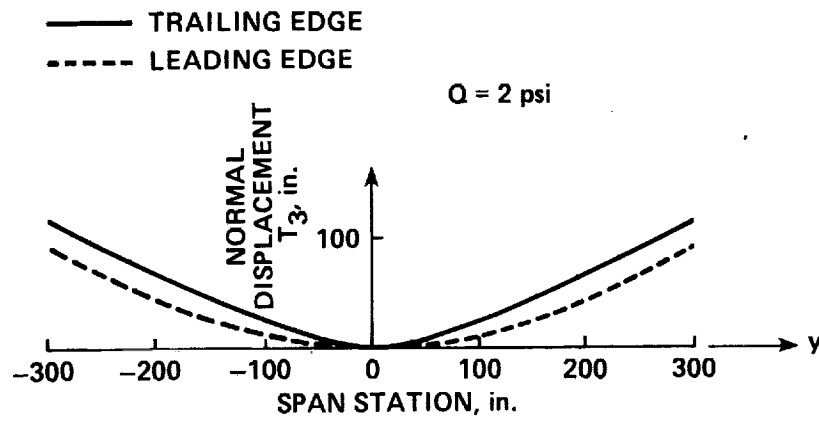
Figure 5.- Displacement in z-direction for swept-back wing.
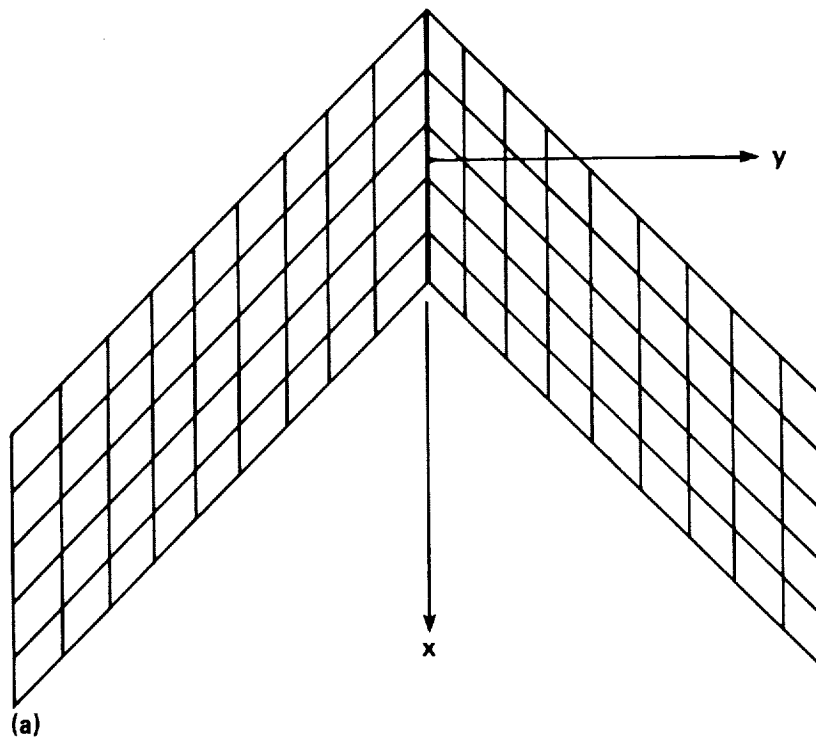
Figure 6(a).- Two-surface spline regions for swept-back wing (surface spline regions are divided by the thick lines).
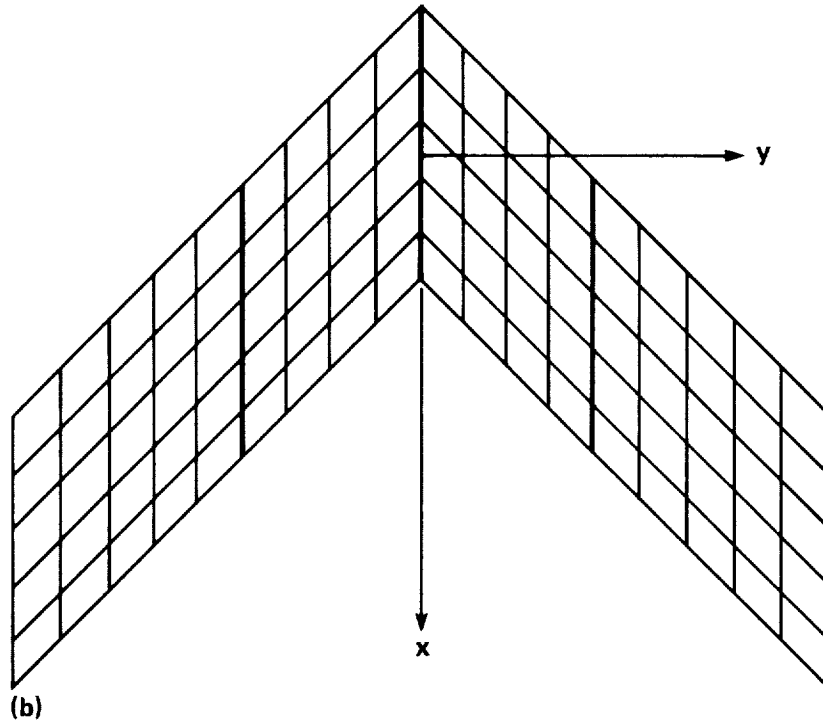
Figure 6(b).- Four-surface spline regions for swept-back wing.
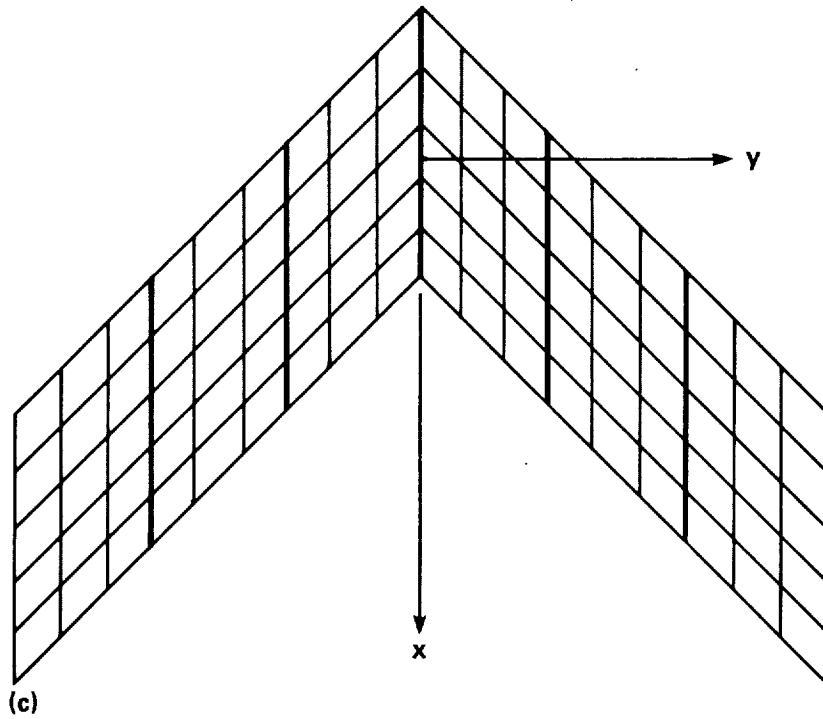
Figure 6(c).- Six-surface spline regions for swept-back wing.
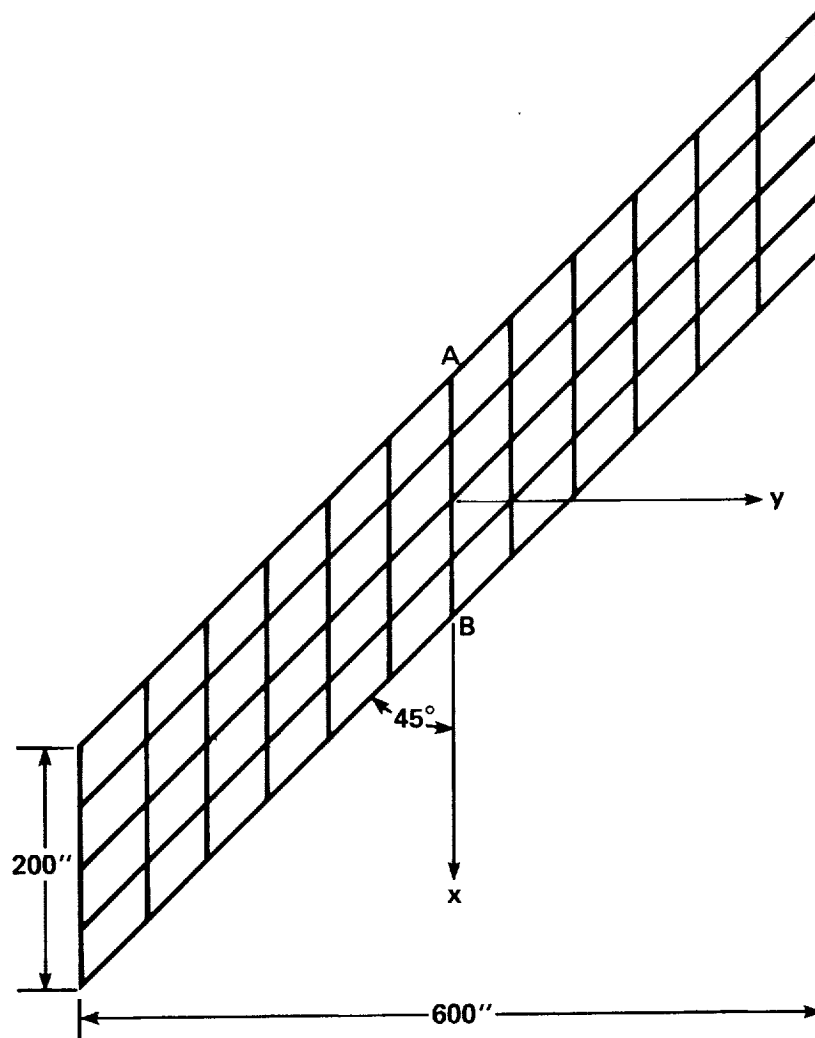
Figure 7.- Structural grid for oblique-wing I.
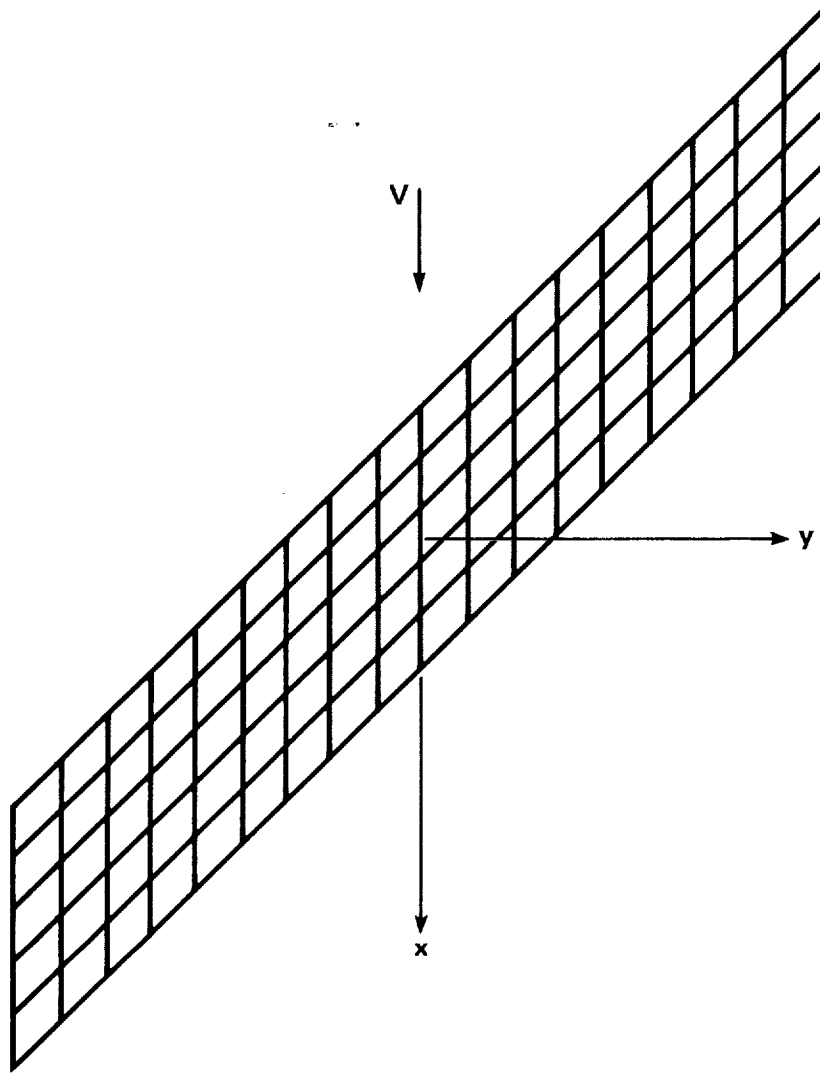
Figure 8.- Aerodynamic grid for oblique-wing I.
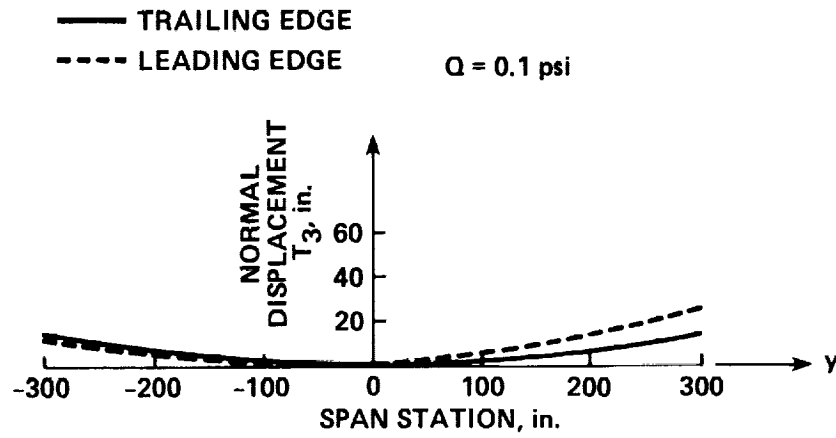
Figure 9.- Displacement in z-direction for oblique-wing I.
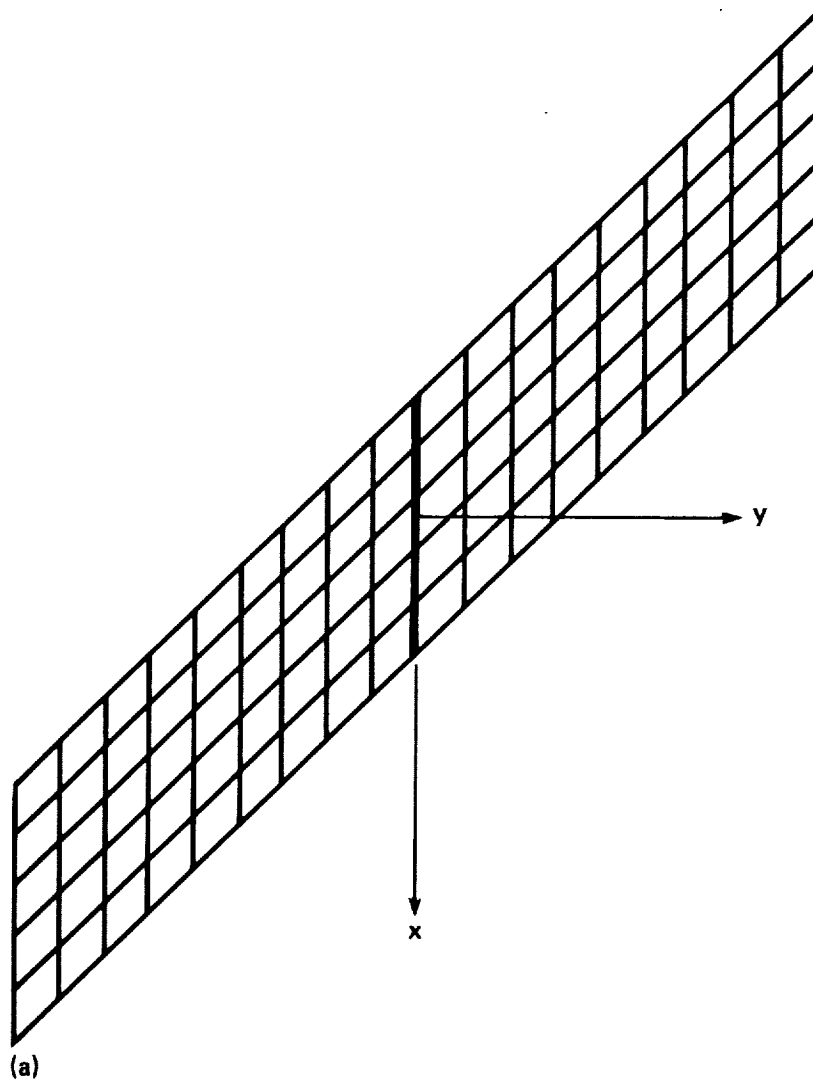
Figure 10(a).- Two-surface spline regions for oblique-wing I.

34
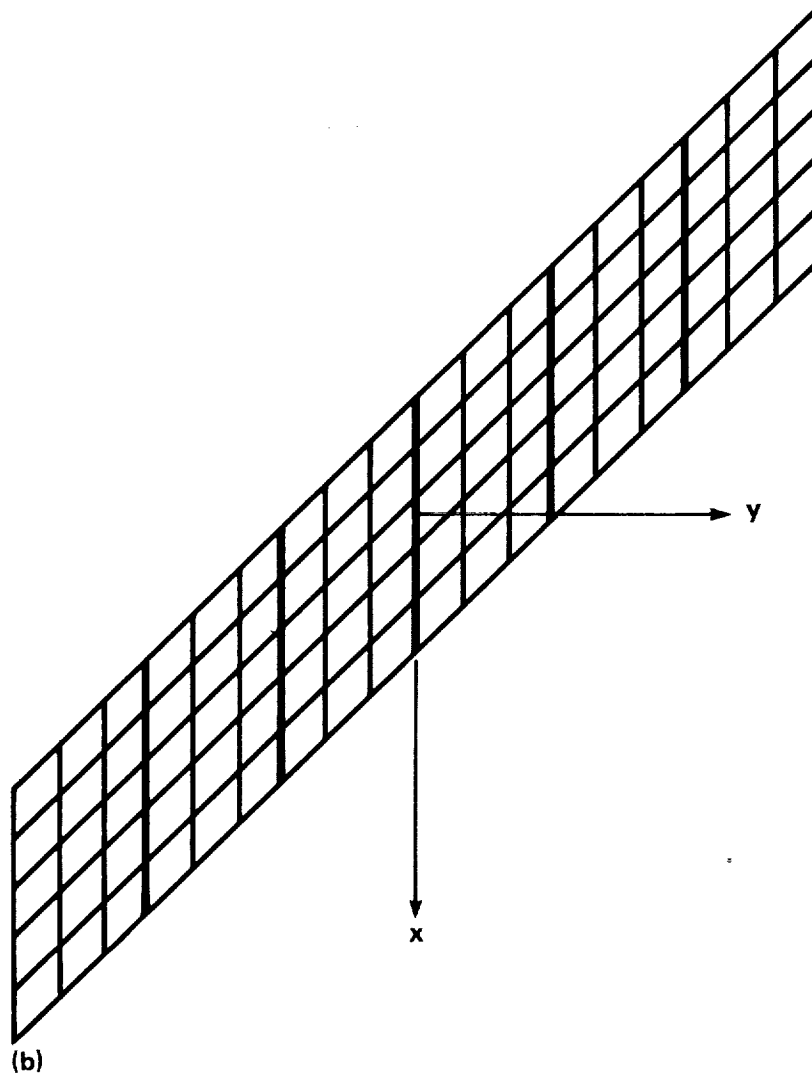
Figure 10(b).- Six-surface spline regions for oblique-wing I.

35
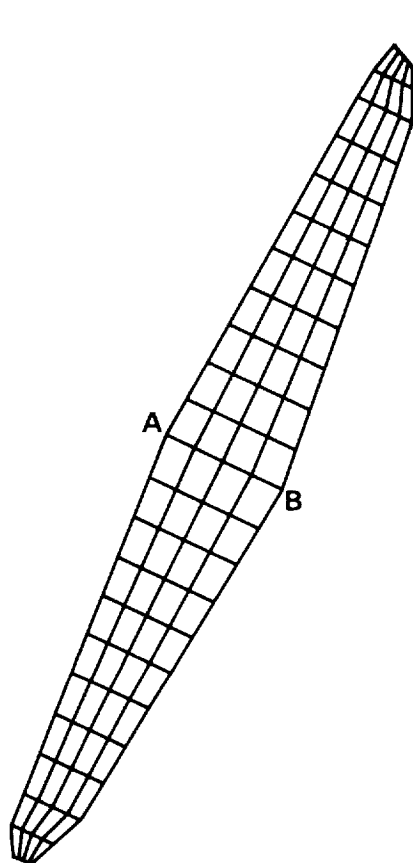
Figure 11.- Structural grid for oblique-wing II (plate model).
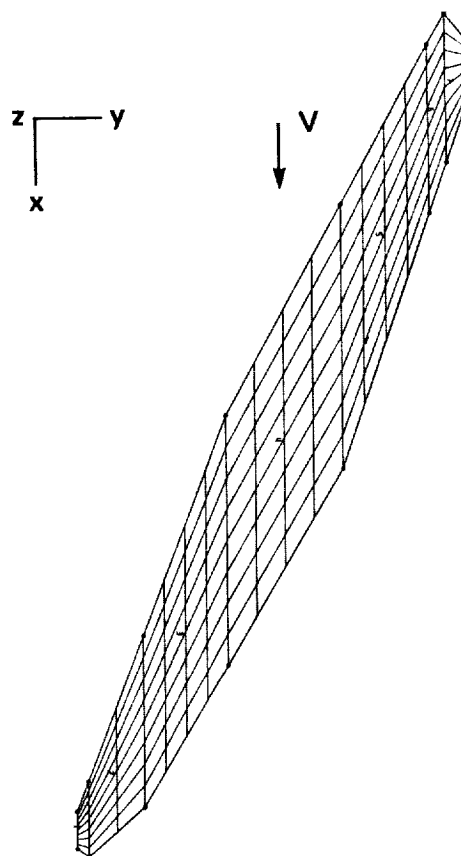
Figure 12.- Aerodynamic grid for oblique-wing II (plate model).
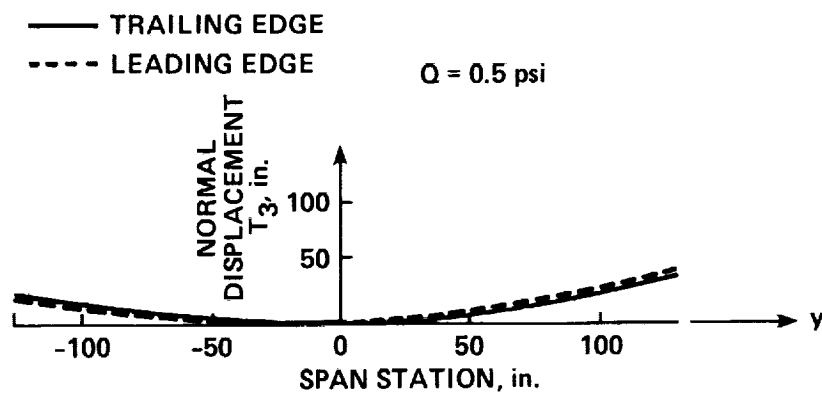
Figure 13.- Displacement in z-direction for oblique-wing II.
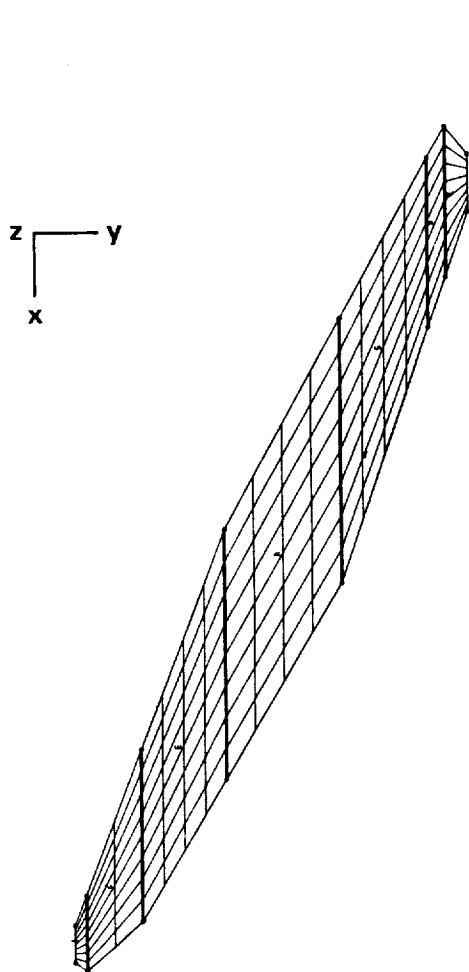
Figure 14(a).- Seven-surface spline
  regions for oblique-wing II (plate
  model), 136 aero elements.
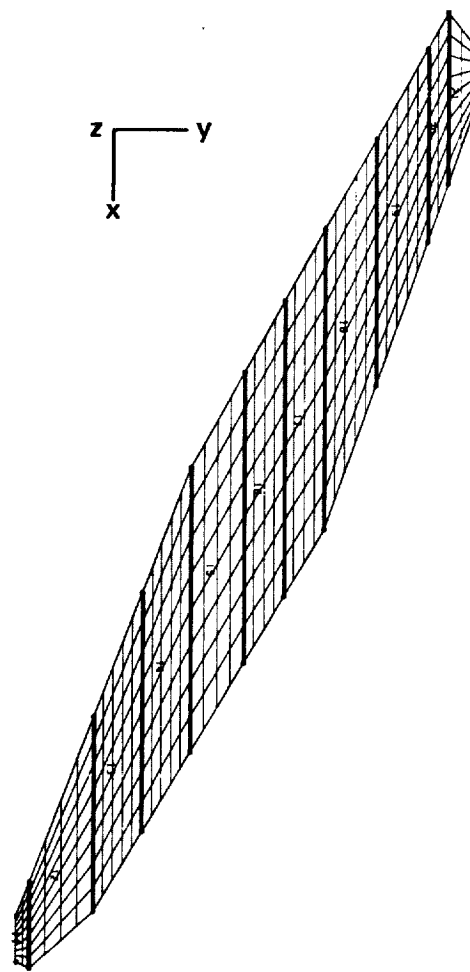
Figure 14(b).- Eleven-surface spline
  regions for oblique-wing II (plate
  model), 336 aero elements.
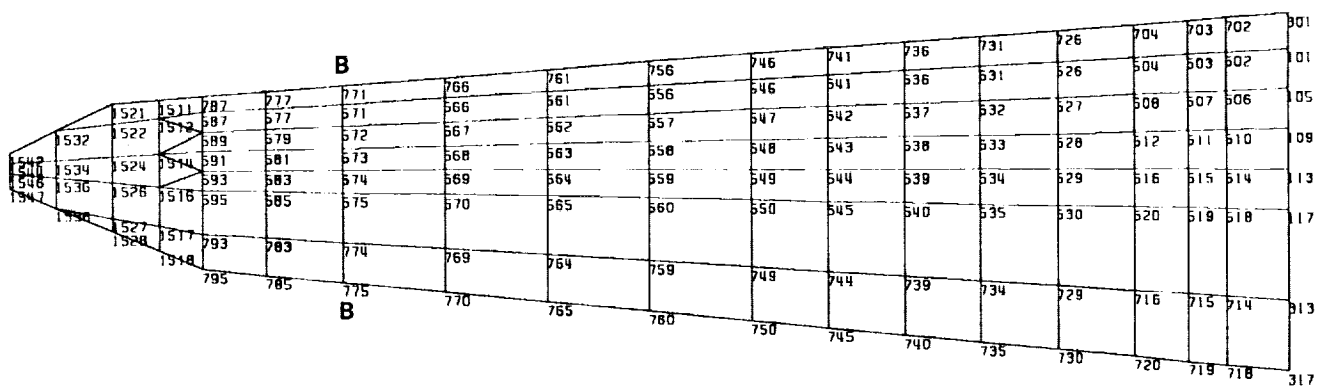
Figure 15(a).- Structural grid for 250 ft^2 baseline oblique wing (upper surface of left wing).
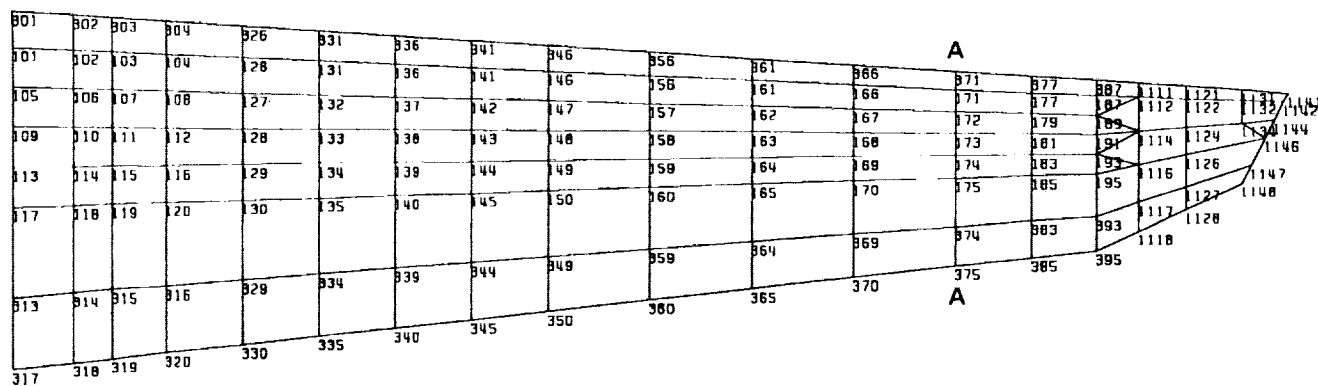
Figure 15(b).- Structural grid for 250 ft^2 baseline oblique wing (upper surface of right wing).

38
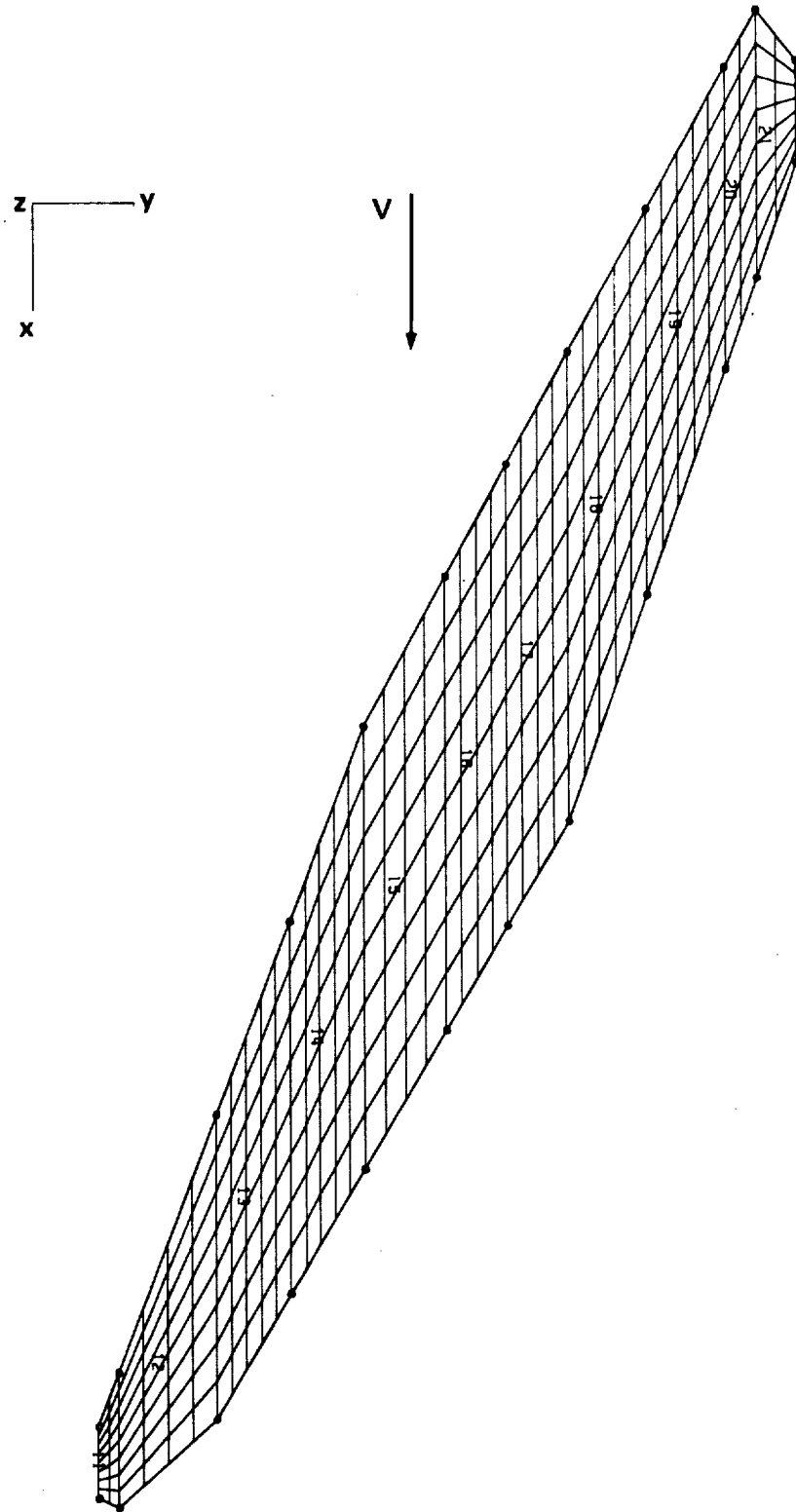
Figure 16.- Aerodynamic grid for 250 ft^2 baseline oblique wing.
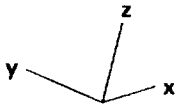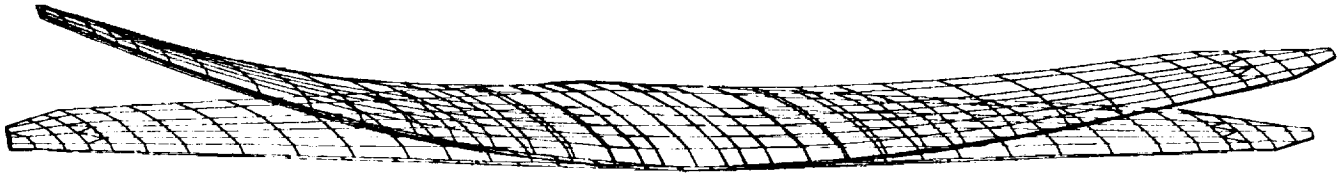
Figure 17(a).- Structural deformation of 250 ft^2 baseline oblique wing.
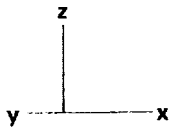
Figure 17(b).- Structural deformation of 250 ft^2 baseline oblique wing.
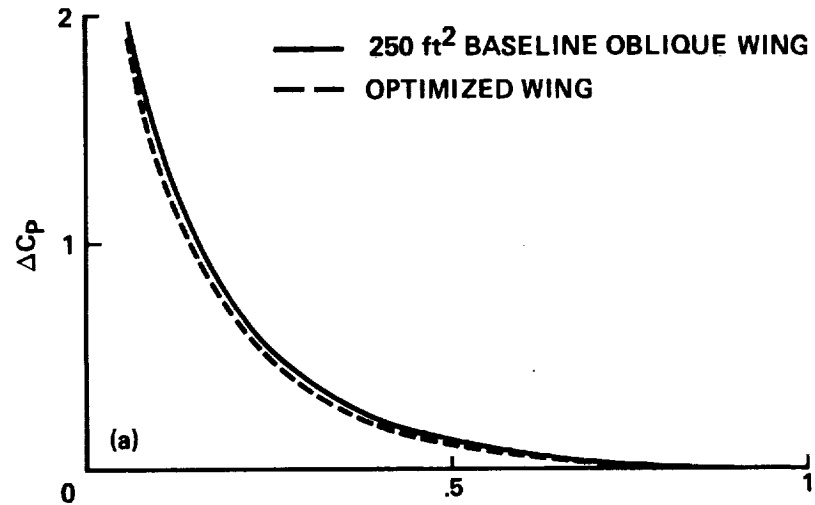
(a) 98.5% aerodynamic semispan station (left wing).
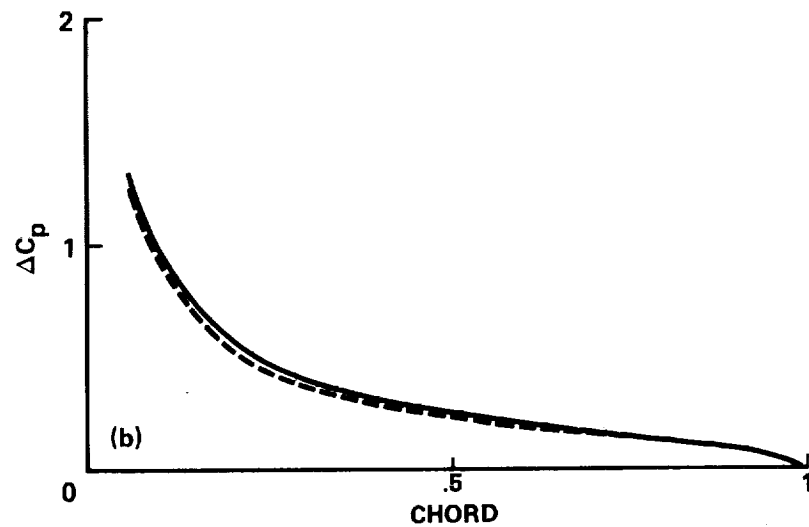
(b) 70.0% aerodynamic semispan station (left wing).

Figure 18.- Comparison of pressure distribution between baseline oblique wing and optimized wing (M = 0.7, α = 10°).

(c) 34.0% aerodynamic semispan station (left wing)
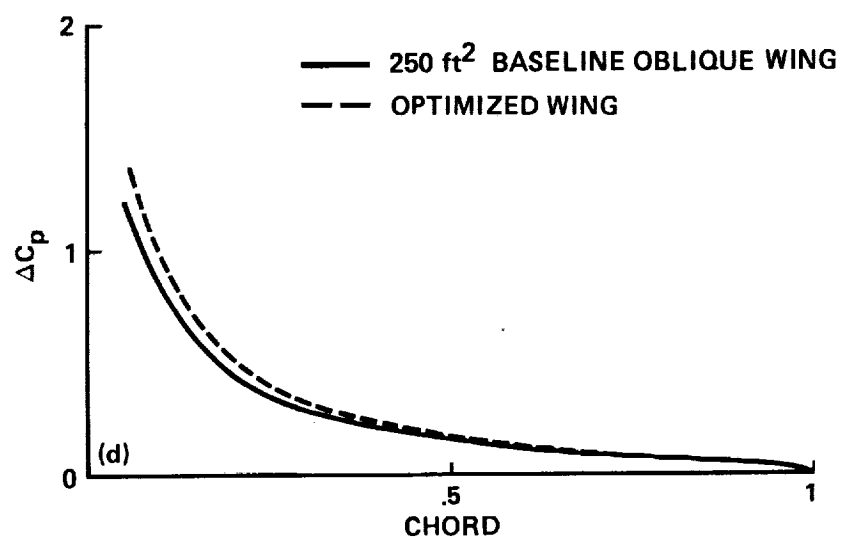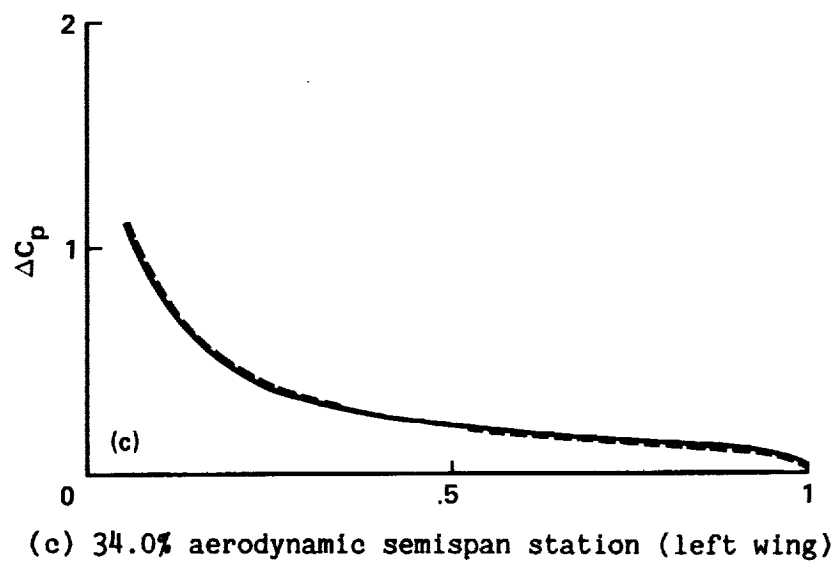
Figure 18.- Continued. (d) 33.0% aerodynamic semispan station (right wing).
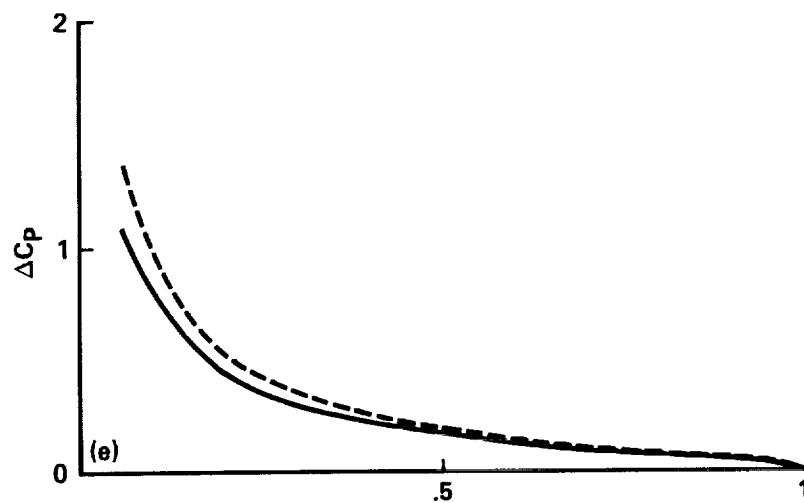
(e) 71.0% aerodynamic semispan station (right wing).
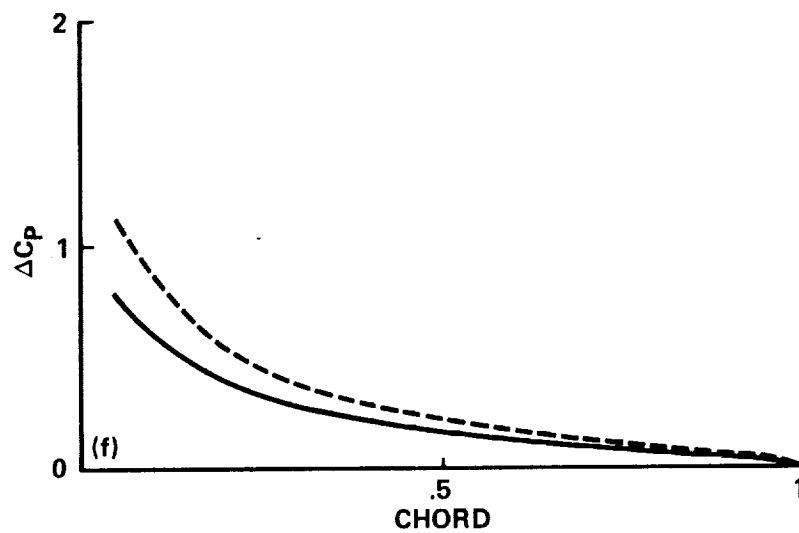
Figure 18.- Continued.   (f) 86.5% aerodynamic semispan station (right wing).
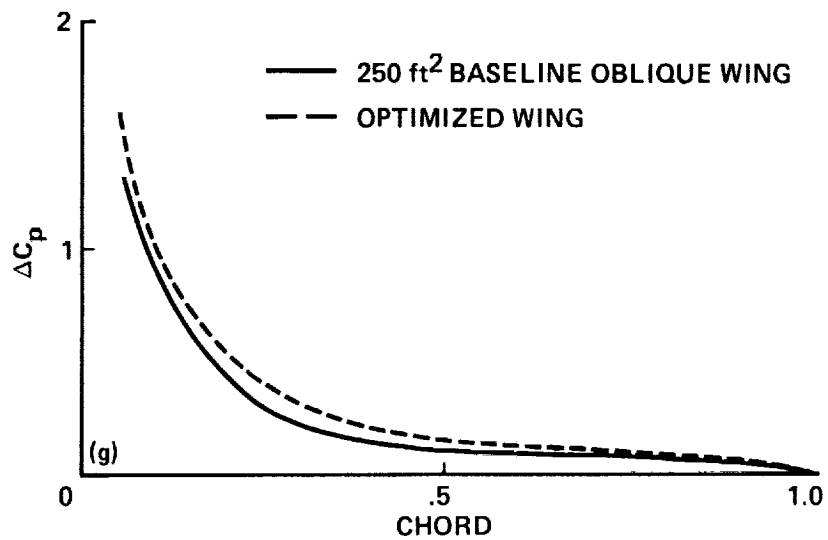
Figure 18.- Concluded. (g) 97.0% aerodynamic semispan station (right wing).
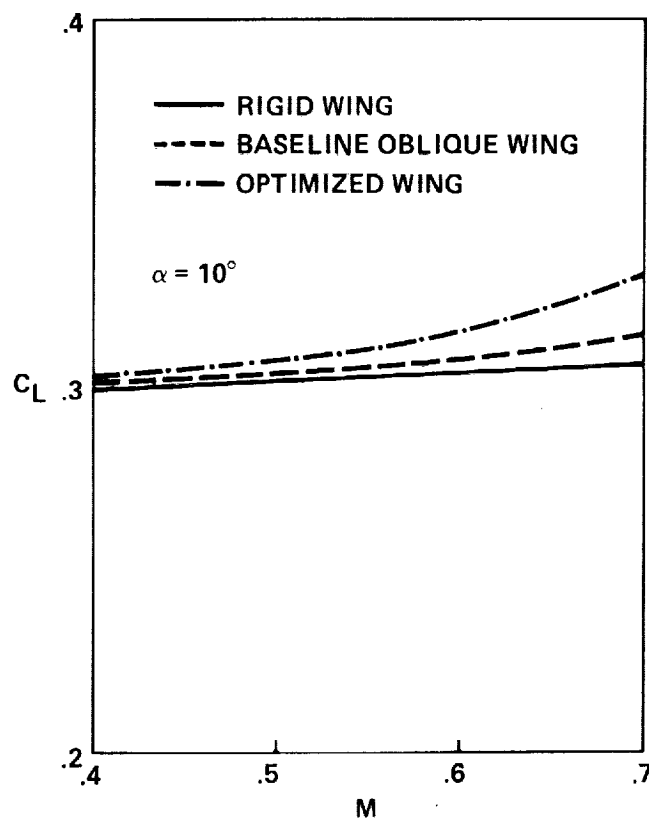
Figure 19.- Lift coefficient versus Mach number (α = 10°).
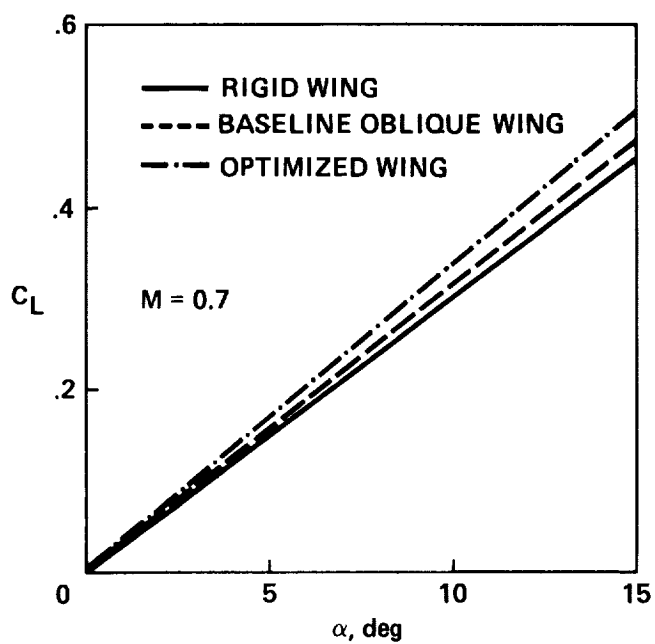
Figure 20.- Lift coefficient versus angle of attack (M = 0.7).
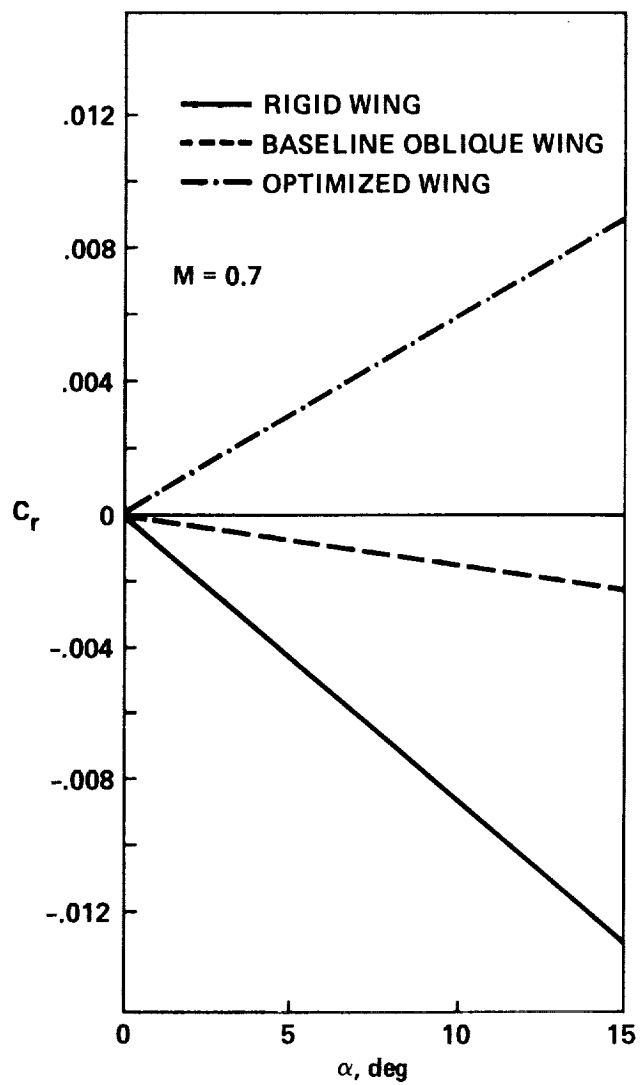
Figure 21.- Rolling-moment coefficient versus angle of attack (M = 0.7).
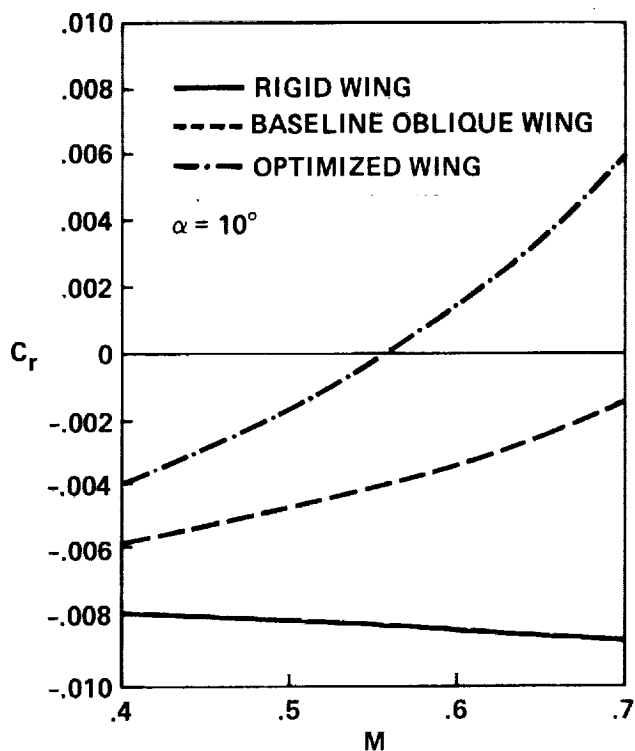
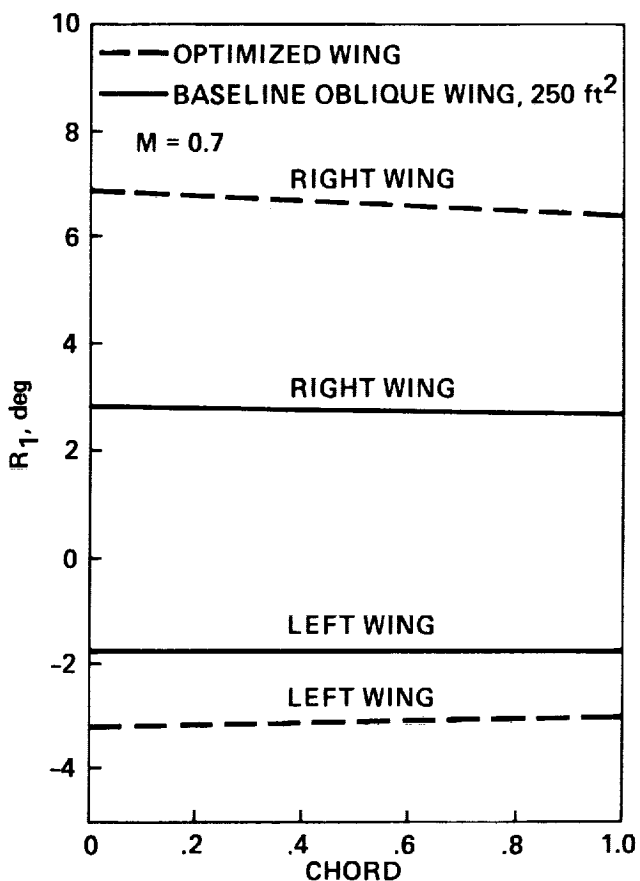Figure 22.- Rolling-moment coefficient versus Mach number (α = 10°).

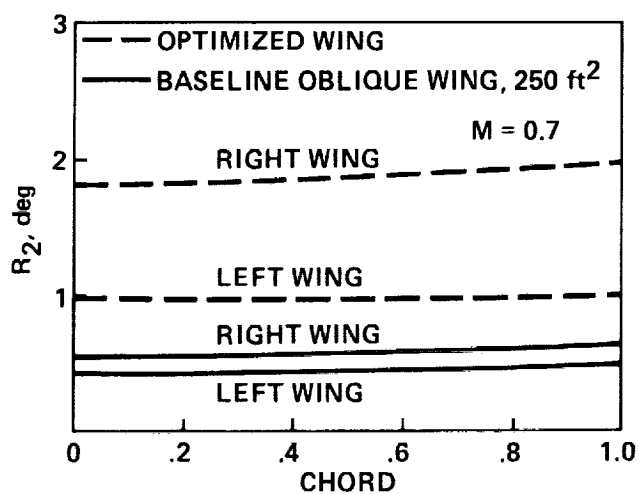Figure 23.- Bending angle of deformed wings (74% span station).

Figure 24.- Twisting angle of deformed wings (74% span station).
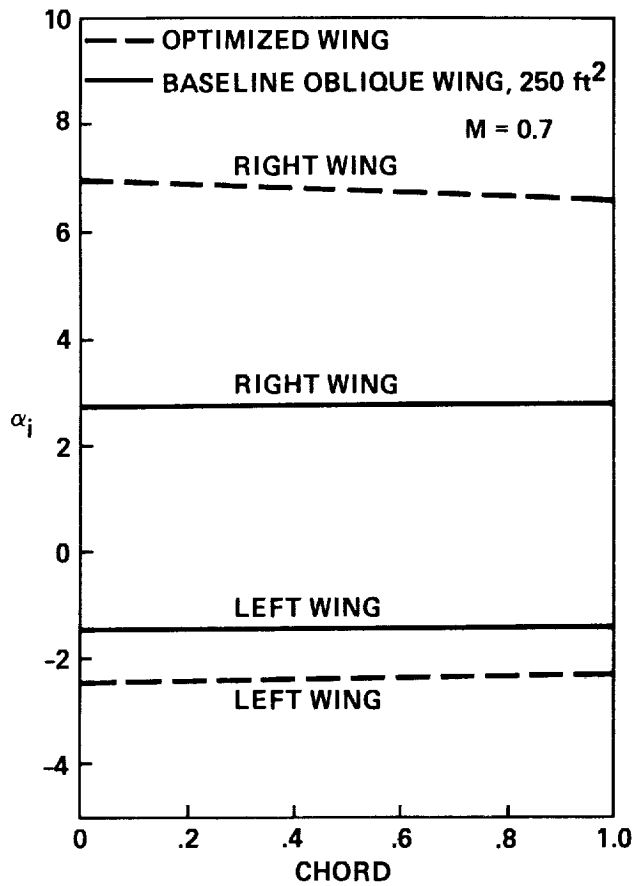
46

Figure 25.- Local angle-of-attack change caused by wing twisting and bending (74% span station).
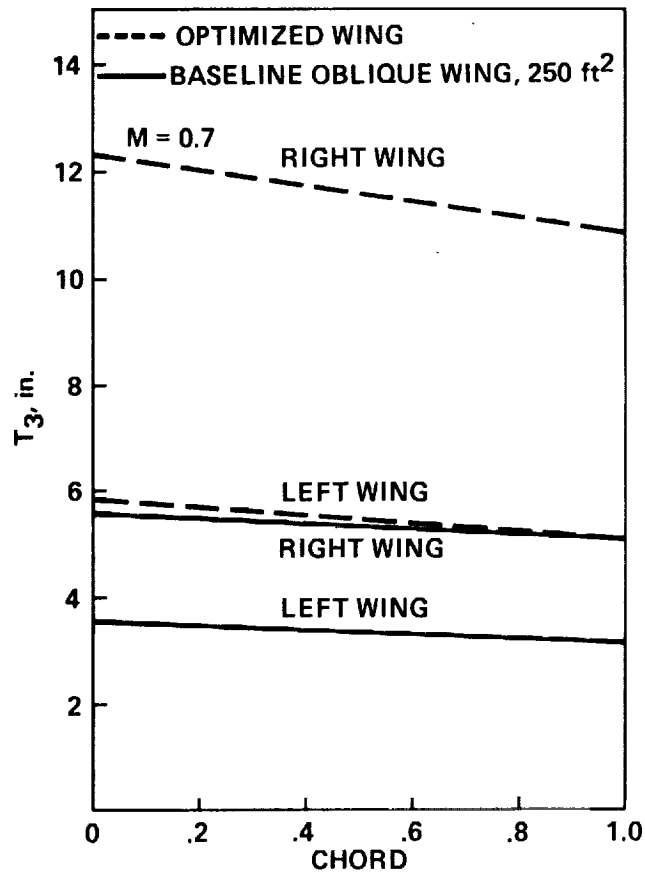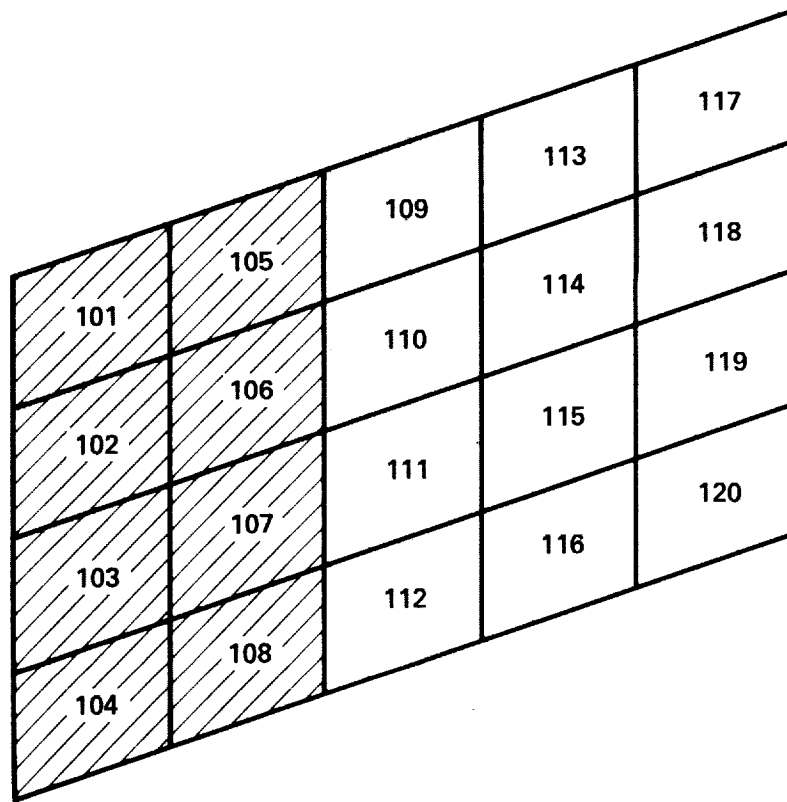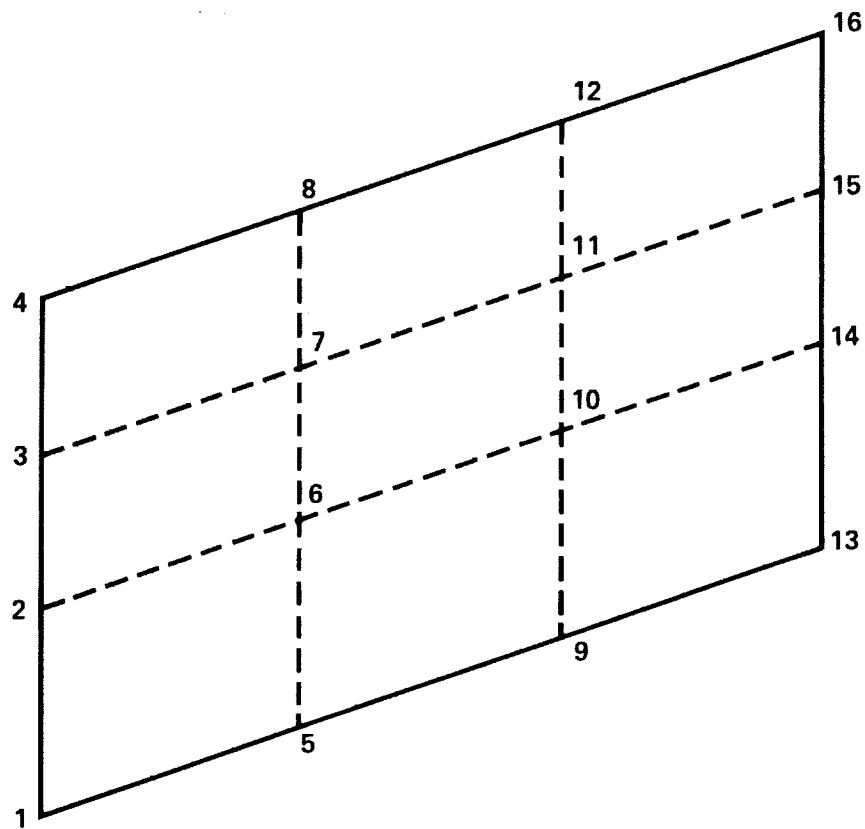

Figure 26.- Vertical displacements of deformed wings (74% span station).

AERODYNAMIC ELEMENT

STRUCTURAL ELEMENT

Figure 27.- Aerodynamic and structural elements for interpolation.

NASA National Aeronautics and Space Administration	Report Documentation Page		
1. Report No. NASA TM-89423	**2. Government Accession No.**	**3. Recipient's Catalog No.**	

4. Title and Subtitle Static Aeroelastic Analysis for Generic Configuration Aircraft	**5. Report Date** June 1987
	6. Performing Organization Code

7. Author(s) In Lee, Hirokazu Miura, and Mladen K. Chargin	**8. Performing Organization Report No.** A-87091
	10. Work Unit No. 533-06-01

9. Performing Organization Name and Address Ames Research Center Moffett Field, CA 94035	**11. Contract or Grant No.**
	13. Type of Report and Period Covered Technical Memorandum
12. Sponsoring Agency Name and Address National Aeronautics and Space Administration Washington, DC 20546	
	14. Sponsoring Agency Code

15. Supplementary Notes

Point of Contact: H. Miura, Ames Research Center, M/S 237-11
Moffett Field, CA 94035 (415) 694-5888 or FTS 464-5888

16. Abstract

A static aeroelastic analysis capability that can calculate flexible air loads for generic configuration aircraft was developed. It was made possible by integrating a finite element structural analysis code (MSC/NASTRAN) and a panel code of aerodynamic analysis based on linear potential flow theory. The framework already built in MSC/NASTRAN was used and the aerodynamic influence coefficient matrix is computed externally and inserted in the NASTRAN by means of a DMAP program. It was shown that deformation and flexible airloads of an oblique wing aircraft can be calculated reliably by this code both in subsonic and supersonic speeds. Preliminary results indicating importance of flexibility in calculating air loads for this type of aircraft are presented.

17. Key Words (Suggested by Author(s)) Aeroelasticity, Oblique wing, NASTRAN, Static aeroelasticity	**18. Distribution Statement** Subject Category - 07		
19. Security Classif. (of this report) Unclassified	**20. Security Classif. (of this page)** Unclassified	**21. No. of pages** 53	**22. Price** A04

NASA FORM 1626 OCT 86